Iron Zinc Selenide Binary Metal Nanosheets for Supercapacitors

By

Ayesha Ishfaq

School of Chemical and Materials Engineering

National University of Sciences and Technology

2022

Iron Zinc Selenide Binary Metal Nanosheets for Supercapacitors

Ayesha Ishfaq

Reg. No: 275994

This thesis is submitted as partial fulfillment of the requirements for the degree of

MS in Nano Science and Engineering

Supervisor Name: Dr. Aftab Akram

School of Chemical and Materials Engineering (SCME)

National University of Sciences and Technology (NUST)

H-12 Islamabad, Pakistan

June, 2022

DEDICATION

I dedicate this thesis to my beloved parents, who have always taught me to believe in Allah Almighty, believe in the hard work and continuously supported me throughout my academic career. My teachers, who are a great source of inspiration and motivation. Their sincere guidance guided my way clearly. My friends and family, who have been a constant source of support and encouragement during the challenges.

Acknowledgments

"In the name of Allah, the Most Merciful and Beneficent." All praise and thanks be to Allah, the Lord of the 'Alamin. First and foremost, I am grateful to ALLAH ALMIGHTY, who has blessed me with good health, abilities, and courage to perform and complete my work successfully; without ALLAH's help, I would not have been able to complete my work completely.

I'd want to express my heartfelt gratitude to my supervisor, Dr. Muhammad Aftab Akram, one of my admired personalities, for his clear and effective instruction, assistance, counsel, and encouragement in completing my project and thesis. His calm and humble demeanour inspired me to give it my all.

I am grateful to my co-supervisor, Dr. Zeeshan Ali for his hard work, dedication, showing an interest in my study topic and providing expert advice and suggestions on how to improve it.

I would like to express my gratitude to Dr. Sofia Javed and Dr. Mohsin Saleem, members of my guiding committee, for their assistance with my work.

I am grateful to Dr. Amir Azam Khan, the Principal of SCME, for allowing me to conduct my study in this subject. I have no words to express my gratitude to Dr. Khurram Yaqoob, the Head of Department of the Materials Engineering department, for creating a conducive research atmosphere. I'd want to thank everyone of the SCME faculty for their cooperation.

I would like to thank my friends and seniors, Mr Muhammad Ali, Mr Usman Hayder, Mr. Tayyab Ahsan, Mr. Muhammad Usman, Mr. Arman Liaqat, Mr. Adeel Akram, Ms. Mahrukh Rahman, Ms. Hafsa Afzal who have helped during characterization and guided me throughout my research work.

I am thankful to my department SCME, for providing me support and such a platform to help me perform my experiments throughout my research work.

During my research experience, I appreciate the financial and technical assistance offered by our department, SCME, which made this project work unforgettable. Last but

not least, I want to express my gratitude to my family for their prayers, support, and faith in me, without which I would not have been able to achieve my full potential.

Abstract

Due to strong conductivity and high electrochemical activity, transition metal selenides (TMSs) have gotten a lot of attention in the field of electrochemical energy storage. TMSs have sufficient energy capacities, outstanding rate capabilities, prolonged and stable life. Introduction of binary metal combination in these materials further enhances their intrinsic conductivity and renders their suitability for electrochemical charge storage. In an effort to produce an economical combination of Binary-Transition Metal Selenides (termed as B-TMSs), herein, we report a simple, straightforward, and thorough technique. Hence, nanosheet like nanostructures of B-TMSs were obtained where iron and zinc are the metallic constituents. The morphological, structural, and surface chemistry of nanosheets have all been well investigated. The electrochemical investigation of (FeZnSe termed as FZSe) nanosheets reveals exceptional performance in supercapacitor application. The FZSe electrode exhibited a particular response due to the synergistic impact of Fe and Zn with a maximum specific capacitance (C_{sp}) of 1140 Fg^{-1} at a current density of 0.5 Ag^{-1}, cyclic stability of 75%, and coulombic efficiency of 100% over 5000 cycles. Asymmetric supercapacitor made of FZSe nanosheets demonstrated a high-power density of 1440 Wkg^{-1}, energy density of 10.6 $Whkg^{-1}$, coulombic efficiency of 93%, and capacitance retention of 83.5% over 7000 cycles. Because of its high surface area, nanosheets shape and mixed transition metal selenide synergetic effect, the asymmetric supercapacitor has a lot of potential for practical supercapacitors.

Table of contents

List of Figures

List of Tables

List of Abbreviations

FeSe ---------- Iron Selenide

ZnSe ---------- Zinc Selenide

FeZnSe ---------- Iron Zinc Selenide

CTAB----------CetylTriammoniumBromide

CV ---------- Cylic Voltammetry

GCD----------Galvanostatic Charge-Discharge

EIS----------Electrical Impedence Spectroscopy

TMSs----------Transition Metal Selenides

BTMSs----------Binary Transition Metal Selenides

SEM----------Scanning Electron Microscopy

TEM----------Transmission Electron Microscopy

XRD----------X-ray Diffraction

BET----------Brunauer-Emmett-Teller

Chapter 1
Introduction

1.1 Introduction

There is severe energy crisis going on in the world. The transition to environmentally friendly and sustainable energy sources is urgently needed [1, 2]. The world's energy supplies are diminishing day by day as a result of rising human population and increased energy use. The reliance on fossil fuels such as coal, gas, and oil is increasing at an alarming rate. As a result, fossil fuels are rapidly depleting. Furthermore, the combustion of these materials produces gases such as CO_2, SO_x, and NO_x, which not only pollute the environment but also pose a threat to human life on Earth due to global warming and the greenhouse effect. Environmental and water pollution has become extremely dangerous to human life. This pollution is causing harm to people's health [3]. Heavy metals and organic dyes are two pollutants that damage the environment and contribute to major health problems. Due to the limited capacity of automatic cleaning and the addition of untreated industrial waste to these bodies of water, water pollution has developed into a global natural phenomena. Maintaining a green and cleaner atmosphere is critical. Renewable energy resources have been concentrating their efforts on resolving the energy issue caused by the reduction of nonrenewable energy resources such as fossil fuels and petroleum. Numerous resources are being tapped that do not alone generate green energy but are also in low cost [4]. To develop environmentally friendly and green items that will prevent these energy harvesting devices from polluting the environment. Numerous materials and devices have been synthesized since then solar cells, wind turbines, fuel cells, and capacitors have all been manufactured supercapacitors, which are capable of not only generating renewable energy but also storing it for long durations [5-8]. Renewable energy resources can be reused. They can be used because they are better and natural and also low-cost and as the technology is improving, new techniques are being explored. Some of which include wind energy [9], solar energy [10-12] and hydrothermal energy [13].

The demand for smart energy storage devices in today's era is on the peak with the rapid development of industries in the past few years [14, 15]. Advanced electrical energy storage devices with both high energy storage and high power output performances are needed to meet the critical applications.[16, 17] Energy storage devices are required for energy conversion devices to perform properly and store energy because of the increase in the demand of renewable resources and energy . A considerable effort has been conducted in generating efficient energy storage devices. The lightweight and environmentally friendly flexible electronics control over the current market for a variety of applications such as automobile, displays, LEDs, wearable devices [18]. Energy conversion and storage devices play an important role in the development of new sustainable technologies which requires efficient energy storage systems including rechargeable batteries, supercapacitors and fuel cells.[19, 20] With energy conversion devices, the most frequently used are batteries including Sodium ion batteries, Zinc ion batteries, Lithium ion batteries, Lithium sulfur batteries, Lithium –air batteries. Another important and highly efficient energy storage device is supercapacitor. Supercapacitors hold great promise for fast processing, rapid charging-discharging, and long-term charging/discharging cyclic stability up to millions of cycles. In supercapacitor charge storage phenomenon is different as compared to batteries. The first supercapacitor was fabricated in 1957[18, 21]. Carbon-based electrode material was used which provides high surface area for charge accumulation on the surface. The major drawback of utilizing supercapacitor was that they had low energy density as compared to batteries. Batteries use faradic reactions in the process. For supercapacitors, asymmetric devices are emerging as a new candidate for energy storage. Asymmetric devices in supercapacitors as well as batteries are storing charges by using the phenomena of electrostatic charge storage and faradic reaction. By using both the phenomenon in a single device, as a result, asymmetric devices are able to store high power and energy density.[22, 23] SCs observed various application prospects due to their superior power density, tiny volume and lifespan but they exhibit small specific capacitance and low operating voltage. To overcome this issue, researchers are creating new kinds of electrode material having high specific capacitance or the operation voltage window and electrochemical performances.[13, 24]

1.2 Energy Storage

Energy storage systems are further divided into following categories

- Mechanical system
- Chemical system
- Electrochemical system
- Electrical system
- Thermal system [25]

The two main candidates for electrochemical energy storage devices are batteries and supercapacitors. The two basic phenomena used for storing electrochemical energy in devices are faradic ion exchange and electrostatic charge accumulation on the surface of the electrodes. The electrochemical devices consist of a cathode, an anode, electrolyte, and a separator. The energy that is stored in electrochemical devices is released by ions and electrons movements from electrodes of the device.[20]

1.3 Energy storage devices

Fig 1-1 shows the current state of devices which are being used as energy storage.

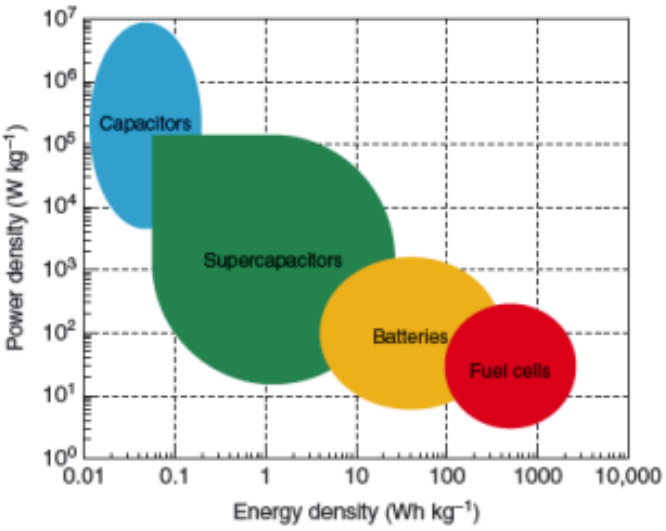

Figure 1-1 Ragone plot of energy storage devices[26]

1.3.1 Batteries

With the fast development in renewable energy conversion devices, the demand for energy storage media is increasing day by day. Various types of batteries are being used for energy storage applications. The two main categories are as follows.

(i) Primary batteries

(ii) Secondary batteries

1.3.1.1 Primary batteries

Primary batteries, also called 'disposable batteries', used in portable devices which still use the basic idea of a voltaic pile. The electrochemical energy produced by the decomposition of the electrolyte and electrode material will be broken once the electrode or the electrolyte starts degrading. It is only one-time chargeable device. Since this procedure is irreversible, the battery needs to be replaced by a new battery. They are further classified in different types based on electrolyte being used. They use aqueous and non-aqueous, both types of electrolytes [27].

1.3.1.2 Secondary batteries

Secondary batteries are rechargeable batteries which can be charged for multiple numbers of times. They are also known as electrochemical cells. It has a combination of cells in which cell reactions are reversible. By charging from the external and passing the current to flow into it, the chemical conditions within the cell can be restored. They are used in various fields such as transport, electronic devices, solar cell operations. With the development in the electrode materials being used in these devices, the development in these batteries emerged. They are further classified in different types on the basis of electrode material i.e. Lithium-ion batteries and Lead batteries [28]. Figure 1.2 shows the working mechanism of batteries.

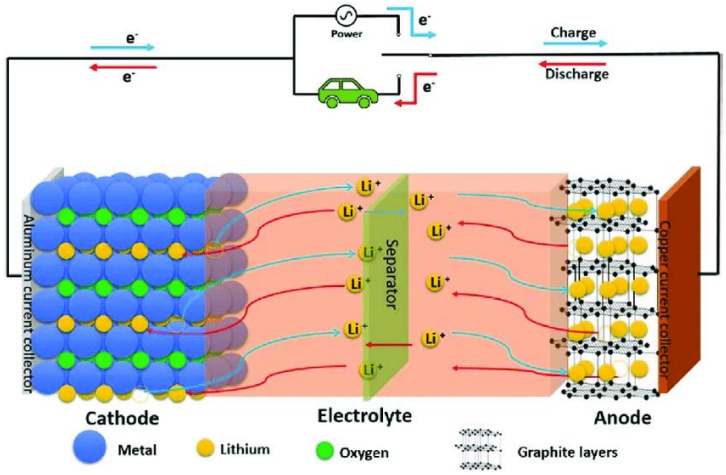

Figure 1-2 Schematic of working batteries

1.3.2 Fuel cells

Fuel cells typically known as energy conversion devices, converts the chemical energy of a fuel and oxidizing agent (typically oxygen) into electricity through multiple redox reactions. To sustain the chemical reaction, it requires a continuous source of fuel and oxygen. These can be further divided into categories based on electrolyte. The ions that are generated during a redox reaction, an electrolyte transfers it from one electrode to the other, making it an essential component of the fuel cells. The electrolytes that are used in a fuel cell are acids, salt carbonates and potassium hydroxide. Some commonly used fuel cells are:

(i) Polymer exchange fuel cell

(ii) Solid oxide fuel cell

(iii) Alkaline fuel cell

(iv) Carbonate fuel cell

(v) Phosphoric acid fuel cell

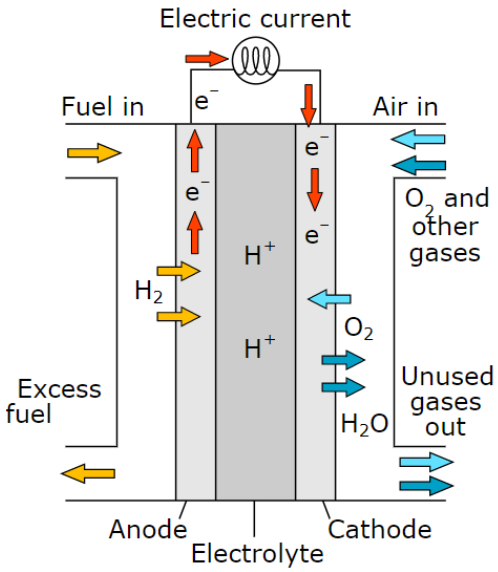

Figure 1-3 Working of a fuel cell

1.3.3 Capacitors

The capacitor is an electrical energy storage device that stores electrical energy in the form of an electric field produced on its electrodes. It is made up of two parallel plates, often known as electrodes, and a dielectric material between the electrodes. Capacitance is defined as a capacitor's ability to store electrical charge, which is computed using the formula

$$Q = CV.$$

The geometries of the electrodes used in the capacitor and the type of dielectric used in the capacitor are used to classify the capacitors into distinct types. The most common type of capacitor is the parallel plate capacitor. Two parallel plates of equal area are arranged parallel to each other in this type. The amount of charge that can be stored is determined by the size of the plates and the dielectric substance employed between them. The formula for calculating its capacitance is

$$C = A / d$$

1.3.4 Supercapacitors

An electrochemical capacitor or an electrolytic capacitor are other names for this type of capacitor. In comparison to fuel cells and batteries, it is the most cost-effective

device for storing energy with a long cycle life and stability. In comparison to electrochemical batteries and fuel cells, it produces a high amount of power while posing less environmental risks. It consists of two electrodes (anode and cathode), an electrode separator, and an electrolyte. The graphic depicts a schematic of a supercapacitor's operation. A supercapacitor's working principle is quite similar to that of a traditional dielectric capacitor. As an external potential difference V is introduced to the electrode, a charge begins to accumulate. Based on the energy storage technique, it is further divided into three types.

i. Electrochemical double layer capacitor
ii. Pseudo capacitors
iii. Hybrid capacitors

Electric double layer capacitors	▪ Carbon aerogels ▪ Activated carbons ▪ Carbon fibers ▪ Carbon nanotubes
Pseudo-capacitors	▪ Metal oxides ▪ Conducting polymers
Hybrid capacitors ❑ **Asymmetric** ❑ **Composite** ❑ **Battery-type**	▪ Carbon materials, conducting polymers ▪ Carbon materials, metal oxides

Figure 1-4 Types of supercapacitors [29].

1.3.4.1 Electrochemical double layer capacitors (EDLC)

The mechanism of charge buildup on the electrode-electrolyte interface is used to store electrical energy in the EDLC. In EDLC, the electrode material's surface area has a significant impact on the device's energy storage capacities. The large surface area ensures optimum contact between the active material and the electrolyte at the interface, allowing charge to be sustained. The electrons flow from the cathode to the anode due to the external applied potential difference, and the cation moves from the anode to the

cathode during the charging process of an electron double layer capacitor. During the discharge process, electrons flow backwards. There is no chemical redox process involved in this sort of supercapacitor. Carbon-based compounds, such as graphite powder, MWCNTs, SWCNTs, activated carbon, and graphene, are the most commonly used materials in EDLC. Figure 1.4 depicts a schematic diagram of how EDLC works.

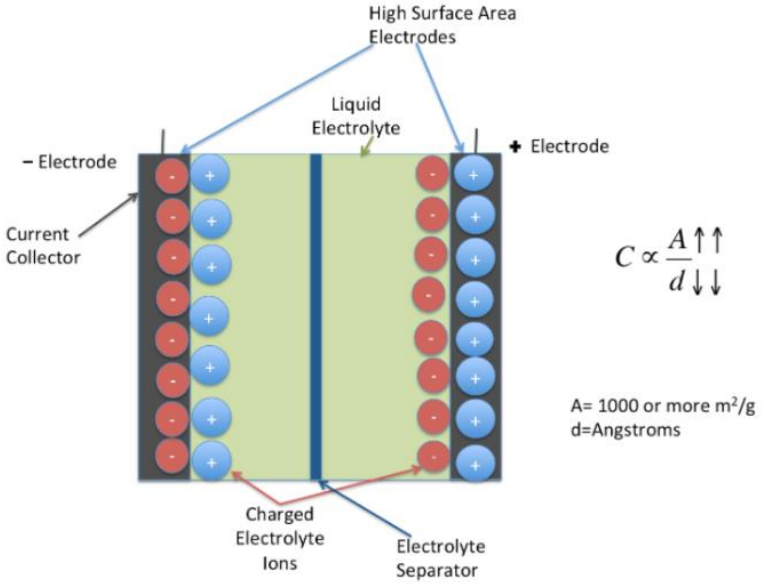

Figure 1-5 Schematic of EDLC supercapacitors

1.3.4.2 Pseudo capacitors

Due to its functioning principle, this type of supercapacitor differs from the EDLC. At the contact of the active substance, chemical redox processes are engaged. The ability to produce a redox reaction under the influence of an externally supplied charge is required for material selectivity for supercapacitor electrodes. Organic compounds (polyaniline and polypyrene), metal oxides (NiO, Co3O4, CuO, and NiCo2O4 etc.), and metal sulfides (MoS2) are among the materials used in pseudo capacitors. Figure 1.5 depicts a schematic diagram of how pseudo capacitors work. The merits of these are energy density, low cost and capacitance.

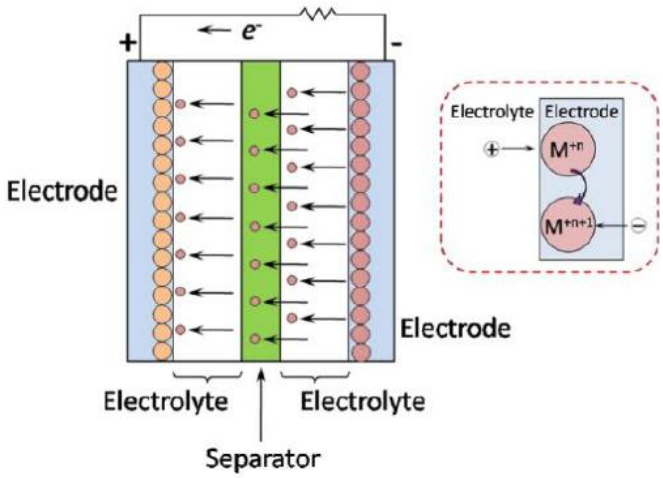

Figure 1-6 Schematic of pseudo capacitors [29].

1.3.4.3 Hybrid supercapacitors

Both pseudo capacitors and EDLCs are used in the design of these supercapacitors. It has two electrodes separated by a semipermeable layer that acts as a separator, preventing electrical contact between them. The electrodes and separator are impregnated with an electrolyte solution that permits ions to pass between them while preventing electrons from discharging the cell.

1.3.4.4 Asymmetric energy storage devices

To attain high energy and power density, asymmetric energy storage devices use both fundamental principles of electron double layer capacitors and batteries. Two different types of electrode materials are used in the asymmetric form of supercapacitors. The first electrode is made up of material that exhibits faradic reaction as an anode, resulting in a high energy density, while the second electrode is made up of capacitor type material, resulting in a high-power density.

1.4 Applications based on supercapacitors

Supercapacitors, because of its quick charging/discharging characteristics and long lifetime of millions of cycles, have become a potential aspirant for energy storage applications. Some of applications of supercapacitors are as follows.

- Integration with Renewable energy converters
- Memory storage systems
- Power electronics
- Photonics
- Robotics
- Spaceships
- Telecommunication systems
- Vehicles

1.5 Literature Review

1.5.1 Supercapacitors based on Carbon

Carbon-based materials are abundant, inexpensive, non-toxic, and simple to produce, with high specific capacitance and good stability [30]. Electric double layer capacitor behavior may be seen in most carbon-based materials. The interface of electrolyte and active substance put on electrode stores electrical charge in these materials. The charge accumulation on the electrode-electrolyte interface is revealed by the CV curve for these materials, which is nearly rectangular [31]. A high surface area with good electrical conductivity is the most important quality to look for when choosing a carbon-based material for a supercapacitor. Carbon nanotubes, graphene, graphite, and carbon fibers all have a huge surface area. Because of its huge surface area, outstanding electrical characteristics, and low cost, activated carbon (AC) is the most often used electrode material. AC can be generated by physically or chemically activating several forms of carbon-containing substances (e.g., wood, coal, nutshell, etc.) [32]. Following the discovery of carbon nanotubes, a huge shift in technology centered on carbon materials occurs. The resistance of the components of a supercapacitor is the major factor that determines the power density. Due to its unique qualities like as porous structure, outstanding thermal, mechanical, and electrical properties, CNTs have gotten a lot of interest as an active material for supercapacitor applications [33]. The activation of porous graphene by KOH was reported by a group of researchers for usage in

supercapacitors[34, 35]. Zhang et al. presented a binary composite of polypyrene nanowire and reduced graphene oxide (PPy-RGO) manufactured via in-situ reduction in the asymmetric device using (Ppy-RGO) composite and high arial capacitance.

1.5.2 Supercapacitors based on Polyaniline (PANI)

Due to their strong conductivity and highly capacitive nature, conducting polymers have gained a lot of attention for usage in energy storage applications as electrode material since 1960.[36] Kaner and his colleagues were the first to employ PANI in supercapacitors. Polyaniline has various advantages over other polymers, including ease of manufacturing and a low cost of specific capacitance. Following Kaner, Rudge et al., a supercapacitor research group, discussed the influence of doping on the performance of PANI in supercapacitor applications.[37] PANI's fundamental flaw is its lack of cyclic stability. Because the electrolyte interacts with PANI, the reactive sites are reduced, resulting in a low specific capacitance.[38] Initially, after the discovery of PANI for use in supercapacitors, the focus of research was to increase the device's electrochemical characteristics and stability. Hu and Chu developed the first practical supercapacitor based on PANI in the early twenty-first century, with an operational potential window of 0.7 V – 0.8 V[39]. PANI's theoretical maximum doping concentration is around 0.5, with a flexible potential limit of 0.7 V and a theoretical capacitance value of 2000 F g^{-1}[40]. Following the doping mechanism, PANI's morphology has a significant impact on its electrochemical performance. PANI's morphology has been controlled by many research groups in order to improve its performance for supercapacitors[41, 42]. The variance in capacitance can be attributed to parameters such as doping levels, structural morphology, and fabrication procedures, according to a significant number of papers on PANI as an electrode material with capacitance varying from 30 to 3000 F g^{-1}. Li et al. created nanostructured polyaniline/sodium alginate composites in bulk, and the electrically polymerized composites had a remarkable specific capacitance of 2093 F $g^{-1}$when compared to the chemically polymerized. Pan [43] researchers group that worked on PANI added a small amount of poly-phenylenediamine during PANI polymerization extended the polymeric chains and improved the specific capacitance and energy storage, according to a group

of PANI researchers. PANI-copper ferrite-acetylene black, a ternary composite of PANI, has previously been reported to have a specific capacitance of 759 F g^{-1} and a power density of 3100 W kg^{-1}[44]. The specific capacitance of 1125 Fg^{-1}has been examined in MoS2/rGO/PANI. The introduction of carbon nanostructures such as graphene and CNTs into contemporary innovations in search of overcoming the stability concerns linked with polymer base electrodes had a positive influence on the overall working of supercapacitors.

1.5.3 Supercapacitors based on Metal Selenide

Transition metal compounds (TMCs) have shown potential as supercapacitor electrode materials by reversing the reaction between their numerous oxidation states [45]. Through a redox interaction between the electrolyte and the active material, supercapacitors store electric energy. Transition metal chalcogenides range from insulators to semiconductors, semimetals to real metals, and have been employed in a variety of applications, including electronics, catalysis, photovoltaics, charge–density waves, and batteries. Due to the high cost of precious metals and the lack of resources, researchers have concentrated on transition metal oxides with high cost-effectiveness, such as manganese dioxide, iron oxide, cobalt oxide, nickel oxide, and tin oxide. Their cycling stability, on the other hand, is inferior to that of noble metal oxides and carbon materials [46]. Because selenium is in the same group as sulfur and oxygen, transition metal selenides exhibit characteristics such as high theoretical capacities, low cost, easy manufacturing that are comparable to sulfides and oxides. Because of the higher density and electrical conductivity of selenium, the volume energy density and rate capability of transition metal selenides as electrode materials may be higher than those of transition metal sulfides and oxide [47]. Transition metal selenides have recently attracted a lot of attention from scientists as electrode materials for electrochemical energy storage devices. A sandwich structure is always observed in transition metal diselenides, with the metal atom at the heart of two selenide layers. Other TMSs (ZnSe, Cu_2Se, and CuSe, for example) are largely semiconducting and have a higher conductivity [48]. Because of their unique electrical properties, these materials have also been used in electrochemical energy storage. Other advantages of transition metal selenides are their low cost, abundant earth, and ease of manufacture; these features are particularly advantageous for

their use in electrical devices. More critically, these properties make transition metal selenides potential electrode candidates for suggested electrochemical energy storage devices[49]. Despite mono metal selenides' exceptional electrochemical performance, there is an urgent need to produce metal selenide-based materials with significantly greater specific capacity and rate capability without sacrificing their cycle performance. Due to the synergistic action of various metal ions, bimetallic metal selenides have garnered considerable interest as possible high capacity electrode materials in this area [50]. Miao et al. [51] demonstrated the capacitive properties of $CoSe_2$ nanosheets grown on Ni foam and encased in N-doped carbon ($CoSe_2$/NCsingle bondNF), a composite formed by carbonising MOF in the presence of Se powder. The Cs of the $CoSe_2$/NCsingle bondNF was 120.2 mA h g^1 at 1 A g^{-1}. Beirong Ye demonstrated a coelectrodeposition approach was used to create a NiSe/ZnSe (NZSe) hybrid nanostructure on a nickel foam substrate as a binder-free electrode for asymmetric supercapacitors that exhibited a capacitance of 651.5 $mAhg^{-1}$at $1Ag^{-1}$ higher than that of pure NiSe (267.5 mAh g^{-1}) and ZnSe (211.1 mAh g^{-1}) at the same current density [52]. HuiPeng, synthesized $Co_{0.85}Se$ and N-PCNs electrodes for an asymmetric supercapacitor. A simple solvothermal approach is used to create petal-like nanosheets. With an operating voltage window of 1.6 V, the aqueous ASC has an energy density of 21.1 W h kg1 and a power density of 400 W kg^{-1} with exceptional cycling stability of 93.8 percent capacitance retention after 5000 cycles.[53] ShangWu synthesized $Ni_{0.85}Se$ nanoparticles. The $Ni_{0.85}Se$/AC ASC operates at 1.65 V, has a high energy density of 22.3 Wh kg^{-1} at a power density of 829 W kg^{-1}, and can maintain a capacity of 76% after 5000 cycles.[54] At a current density of 1 A g^{-1}, specific capacitance achieves 510 F g^{-1} with a capacitance retention of 91 % after 5000 cycles.[55] ChuanXia synthesized highly conductive ternary nickel cobalt selenide electrode optimized asymmetric device operating at 1.8 V has a very high stack energy density of 2.85 mW h cm^3 at a stack power density of 10.76 mW cm^3 and a capacitance retention of 85 % after 10,000 continuous charge–discharge cycles.[56] Self-templated synthesis of N-doped $CoSe_2$/C double-shelled dodecahedra for high-performance supercapacitors was produced by YifangZhang.[57] The specific capacity of LuluDu synthesized Ternary nickel-cobalt selenide nanosheet arrays with better electrochemical performance for hybrid

supercapacitors is 430.87 mA h g^{-1} at 1 A g^{-1} and cycling stability is 85.25% after 3000 cycles.[58]

The literature reviewed above examines the historical perspective, emergence, and mechanics of energy storage in energy storage systems. It also covers the various varieties of supercapacitors that are still used today. There is a thorough discussion of the many types of electrode materials used in ultracapacitors. The development of research into the utilization of metal oxide systems as active electrode materials is discussed. Also mentioned are efforts to produce hybrid electrode materials based on a combination of state-of-the-art electrode materials (polymers, metal oxides, and carbon-based compounds). The issues connected with various supercapacitor performance metrics, such as energy and power density, are discussed. The utilization of the synergistic effect produced by mixing elements of various types is extensively demonstrated.[13]

Chapter 2

Experimental section

2.1 Synthesis of electrode material

For the preparation of electrode materials iron zinc selenide, both mono – metals and binary metal precursors were prepared separately and then the process selenization was carried out.

2.1.1 Iron - monometal precursor nanosheets

Table 2-1 Synthesis of Iron - monometal precursor nanosheets

Material name	**Purity level**	**Company name**
Iron Sulfate Hepta Hydrate	99%	SIGMA
Hexacetyltrimethylammonium bromide (CTAB)	99 %	SIGMA
DI water	99%	

For the synthesis of iron mono metal precursor nanosheets two aqueous solutions were separately prepared. Solution A contained iron sulfate 1 mmol (0.278 g) and cetyl triammonium bromide (CTAB) (0.5 g). All of these were dissolved in 50 ml DI water. Solution B was prepared by dissolving sodium borohydride (0.1 g) in 10 ml DI water. Then, Solution B was injected dropwise into solution A while continuous stirring at room temperature. As the stirring continued, the color of the solution started to change gradually and finally after stirring of 15 – 20 minutes the solution turned into brown color. Obtained product was allowed to settle and after 1 hour the product was washed with ethanol and water repeatedly to remove all the unreactive species. After washing with ethanol in the last round, the solution was dried in vacuum oven at 60 °C for 12 hours. After completion of drying the iron mono metal precursor nanosheets were collected.

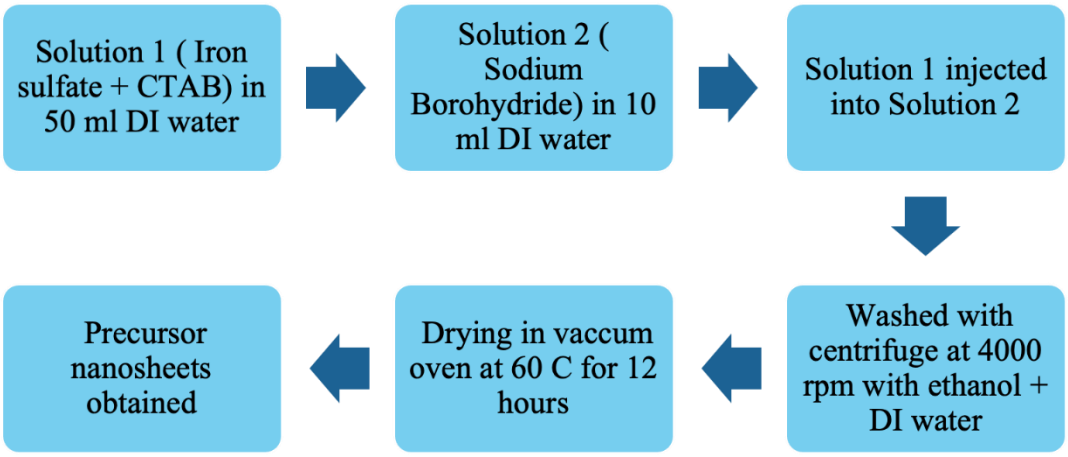

Figure 2-1 Synthesis of Fe precuros nanosheets

2.1.2 Zinc - monometal precursor nanosheets

Table 2-2 Synthesis of Zinc - monometal precursor nanosheets

Material name	**Purity level**	**Company name**
Zinc Sulfate Hepta Hydrate	98%	Riedel-deHaen
Hexacetyltrimethylammonium bromide (CTAB)	99 %	SIGMA
DI water	99%	

For the synthesis of zinc mono metal precursor nanosheets two aqueous solutions were separately prepared. Solution A contained zinc sulfate 1 mmol (0.287 g) and cetyl triammonium bromide (CTAB) (0.5 g). All of these were dissolved in 50 ml DI water. Solution B was prepared by dissolving sodium borohydride (0.1 g) in 10 ml DI water. Then, Solution B was injected dropwise into solution A while continuous stirring at room temperature. As the stirring continued, the color of the solution started to change gradually and finally after stirring of 15 – 20 minutes the solution turned into white color. Obtained product was allowed to settle and after 1 hour the product was washed with ethanol and water repeatedly to remove all the unreactive species. After washing with ethanol in the last round, the solution was dried in vacuum oven at 60 °C for 12

hours. After completion of drying the zinc mono metal precursor nanosheets were collected.

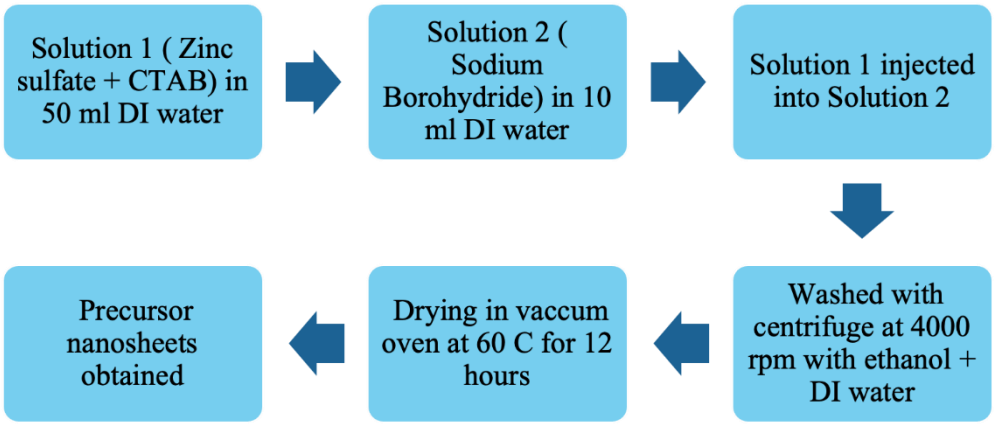

Figure 2-2 Synthesis of Zn precursor nanosheets

2.1.3 Bimetal (Fe Zn) precursor nanosheets

Table 2-3 Synthesis of Bimetal (Fe Zn) precursor nanosheets

Material name	**Purity level**	**Company name**
Iron Sulfate Hepta Hydrate	99%	SIGMA
Zinc Sulfate Hepta Hydrate	98%	Riedel-deHaen
Hexacetyltrimethylammonium bromide (CTAB)	99 %	SIGMA
DI water	99%	

For the synthesis of Bi metal precursor nanosheets two aqueous solutions were separately prepared. Solution A contained Iron sulfate in ratio 0.3 % (0.09174 g), Zinc sulfate in ratio 0.6 % (0.1898 g) and cetyl triammonium bromide (CTAB) 0.5 g. All of these were dissolved in 50 ml DI water. Second solution was prepared by dissolving sodium borohydride (0.1 g) in 10 ml DI water. Then, solution B was injected dropwise into solution A while continuous stirring at room temperature. As the stirring continued, the color of the solution started to change gradually and finally after stirring of 15 – 20

minutes the solution turned into brown color. Obtained product was allowed to settle and after 1 hour the product was washed with ethanol and water repeatedly to remove all the unreactive species. After washing with ethanol in the last round, the solution was dried in vacuum oven at 60 °C for 12 hours. After completion of drying the iron zinc binary metal precursor nanosheets were collected.

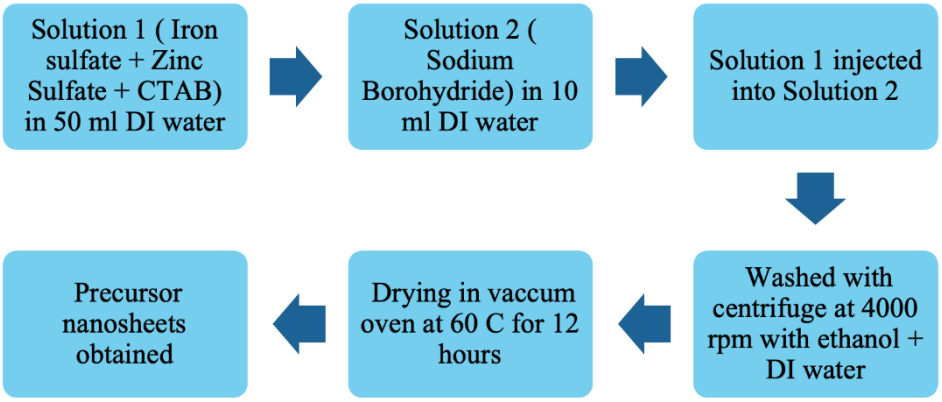

Figure 2-3 Synthesis of Fe Zn precursor nanosheets

2.2 Selenization of precursor nanosheets

Precursor nanosheets were prepared through above-described method. Selenization of precursor nanosheets of both mono metals and bimetals was carried out. The selenization process was carried out by placing powders in a silica glazed ceramic boat using a well ground selenium powder (i.e., weight ratio of 1:2). The boat was covered in Al-foil (with some holes) and selenized at 300°C in an H_2/Ar (10vol% H_2) environment with a 4°C / min ramping rate. Following selenization, the temperature of the furnace was gradually increased to 400°C (2°C/min), and annealing was carried out for 60 minutes before natural cooling to room temperature.

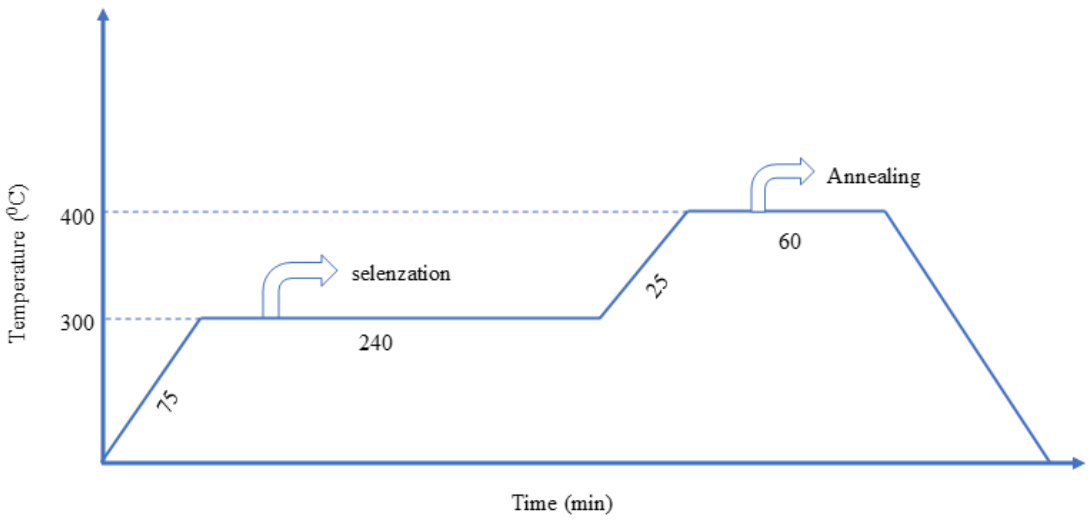

Figure 2-4 Schematic of selenization process

Chapter 3

Characterization Techniques

3.1 X-RAY DIFFRACTION (XRD)

This is extremely valuable for identifying and quantifying crystal phases, as well as the spacing between lattice planes and their distance scale. X-ray wavelengths range from 10 to 8 nm, however the wavelength used for analysis is between 10 and 2.5 nm. Crystallite powder and flat surfaces from organic, inorganic, polymers, metals, and other composites should be used as samples for analysis[59]

Max Von Laue got the Nobel Prize in 1912 for demonstrating that X-rays are diffracted by solid crystals.

There are seven different crystal systems:

- Cubic (isomeric)
- Triclinic
- Tetragonal
- Hexagonal
- Orthorhombic
- Trigonal
- Monoclinic

When X-ray radiation strikes a crystal surface, photons scatter from frequently separated layers of the crystal, resulting in diffraction. If the scattering layers of crystalline solid materials are evenly distributed and the spacing between crystallite layers is of the same length order. The interference occurs in two forms, one constructive and the other destructive, depending on the separation between the planes, resulting in a diffraction pattern [48].

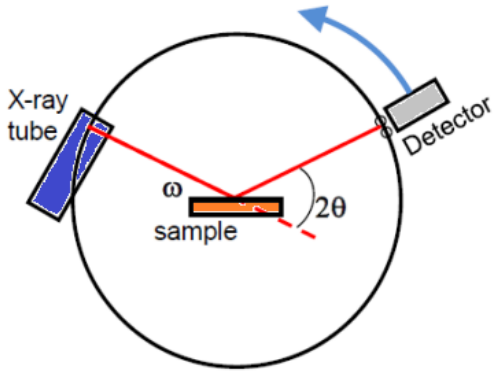

Figure 3-1 Components of XRD

W. H. Bragg and W. L. Bragg developed a connection between scattering angle, layer spacing (d-spacing), and X-radiation wavelength in 1912.

$n\lambda = 2d\sin\theta$

Fig 3-1 shows a basic diagram of X-ray diffractometer. There are five general components that include

- Sample holder
- Radiation source
- Radiation transducer
- Component to limit wavelength range of received radiations
- Signal processing and readout component.

Because the X-ray source and detector are on the same side of the sample in most diffractometers, incident rays strike the sample at an angle, are reflected, and fall onto the detector. When a cathode ray tube's filament is heated, electrons are produced, which are propelled with the help of an applied electric field toward a target, where they collide with the inner shells of the target material to create distinctive x-rays. Copper is the most popular target material for X-ray diffraction, with Cu-K radiation = 1.5418. After that, the monochromatic X-ray beam is focused and pointed towards the sample. The goniometer is the tool that is used to maintain the angle. A scintillation counter is the most common type of detector. The intensity of reflated X-rays obtained via constructive interference is recorded by the detector. X-ray diffractograms are typically counted per second or intensity as a function of 2 degrees, with a scan range of 5 to 90 degrees. Powder X-ray diffraction has a scan range of 5 to 150 degrees [48].

3.2 Transmission Electron Microscopy (TEM)

The shape, crystal structure, and chemical makeup of a sample can all be evaluated using TEM. The image of features is created in this technique by focusing an electron beam on a spot that was transmitted through the specimens. In TEM, a static electron beam with an accelerating voltage of 100kV-400kV interacts with the material and is transmitted. The diffraction pattern is created by electron recombination in objective lenses. An image is created as a result of the electron's contact with the sample, which is then enlarged and magnified and focused by an imaging device such as photographic film.

In comparison to microscopes and scanning electron microscopes, TEM provides a high-resolution image. The following are some of the basic features of TEM, as shown in Figure

- Electron gun
- Specimen holder
- TEM lenses
  - Condenser
  - Objective
  - magnifying
- Viewing chamber
- Camera chamber
- STEM detector

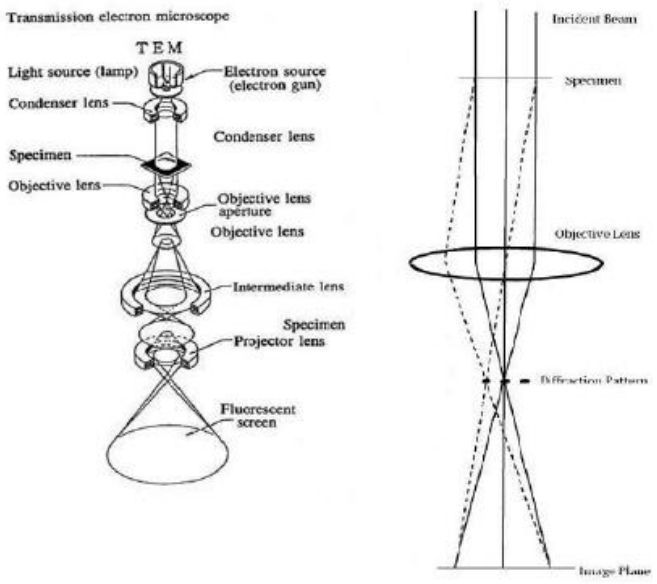

Figure 3-2 Basic schematic of TEM

TEM has further applications which include:

1. **HRTEM**
   1.1. Lattice imaging, Structure of complex materials
   1.2. Interplanar d-spacing
   1.3. Atomic structure of defects
2. **Analytical TEM**
   2.1. Chemical composition
   2.2. Z-contrast imaging
   2.3. Selected area electron diffraction
3. **In-situ TEM**
   3.1. Structural changes
4. **Conventional TEM**
   4.1. Morphology analysis on a nanoscale
   4.2. Phase and defect analysis

3.3 Scanning electron microscope (SEM)

Manfred von Ardenne was the first to design SEM in 1938. A high-energy electron beam is used to create a three-dimensional image of the materials under analysis with a resolution of up to one nanometer. Because it is made up of electromagnets, the

magnification can be adjusted. The object must be conducting to be studied by a SEM, while non-conducting samples are coated with a thin layer of gold, graphite, or aluminium [60]

3.3.1 Working and Construction of SEM

The following are essential components of SEM:

- Electromagnetic lenses
- Electron gun
- Secondary electron detector
- Object chamber
- Display unit.

When an electron gun is heated, it emits a stream of monochromatic electrons that are focused by electromagnetic lenses. By optimizing the amount of electrons in the beam, a condenser lens may control the diameter and current of the beam. The second lens brings the beam together. Finally, the objective lens is used to focus the electron beam on the sample. Scanning coils are used to scan the beam in a grid pattern. The conducting sample is placed on a sample holder that fits into the high vacuum chamber. For improved resolution and particular region analysis, the holder can be moved in the X and Y directions, as well as tilted, rotated, and moved in the Z direction. A secondary electron detector is situated at the back of the sample holder. The surface structure of the material influences the velocity and angle of secondary electrons. When these electrons arrive at the detector, they produce an electronic signal, which is amplified and turned into a digital signal that can be seen on the display unit for further processing [60]

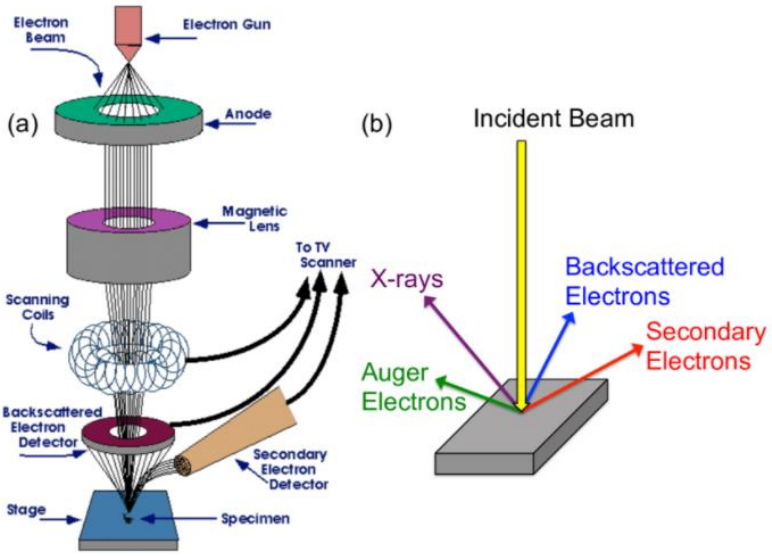

Figure 3-3 (a) Schematic of SEM (b) sample-beam interactions within a SEM.

The interaction of the electron beam with the sample produces a variety of signals. All of these signals provide information about the sample under inquiry in different ways. For imaging, BSE and SE are often employed. SE are used to assess the shape and topography of samples, whereas BSE are used to determine phase separation and are more sensitive to heavier components than SE. In auger electron spectroscopy, AE is employed for surface examination, but in energy dispersive spectroscopy (EDS), the characteristic X-rays are used for elemental and compositional analysis of the sample[59]

3.4 BET Surface Area Analysis

N2 gas is adsorbed or desorbed on the surface of the material in BET analysis, and the multilayer is then monitored as a function of relative pressure on the opposite axis. The equipment is fitted with an automatic analyzer for determining the adsorption or desorption of N2 gas in units of m2 g -1. [33] Physical adsorption of a N2 gas on the surface of the resultant material and manipulation of the 32 amounts of adsorbed gas as a monolayer can be used to determine the specific surface area of a porous material. A volumetric or continuous flow approach is used to determine the amount of gas adsorbed. The adsorption interaction between nitrogen gas and the sample surface is

mostly based on weak van der Waal's interactions, which are carried out at liquid nitrogen temperatures. The BET adsorption isotherm equation is utilized in multi-point BET measurements.

3.4.1 Instrumentation

The components of the BET instrument are as follows:

- Vacuum system and inert gas inlet
- Temperature-controlled system that ranges from very hot to very cold.
- Control chamber for gaseous pressure
- monometer
- Tubes for collecting samples
- Tubes for reference.

At the end of the measurement, both the sample and reference tubes are handled identically. The reference material, such as -alumina powder, should have a large and well-known pore surface area. In a typical BET measurement, the material is degassed by a high-temperature inert gas purge (i.e. 110°C for N2).[61-63]

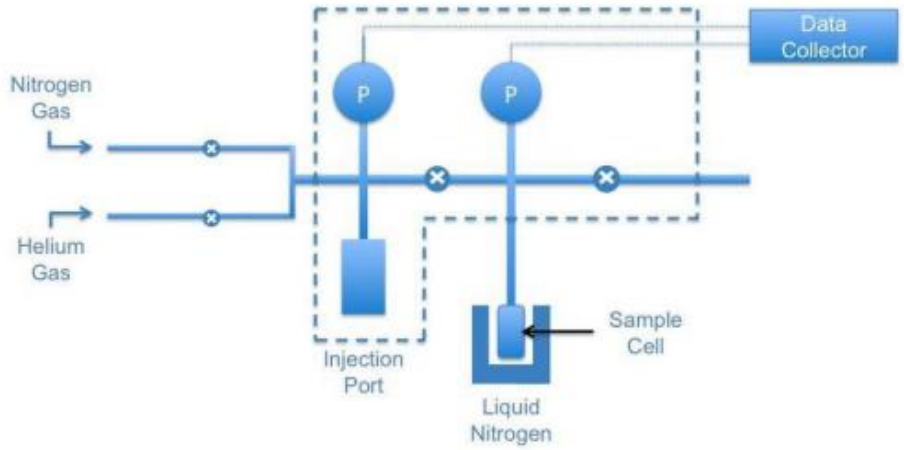

Figure 3-4 Schematic of BET

3.5 Raman analysis

This is a modified kind of FTIR spectroscopy with more efficient properties than FTIR spectroscopy; it is more efficient and non-destructive. This method is most used to identify the functional groups in a molecule. The oscillations of chemical bonds between

atoms are observed using this approach. The atomic mass, atomic radius, electronegativity, and electronegativity of each atom varies. These factors influence the vibrations between atoms. As a result, it generates unique fingerprints for each atom's bond vibrations, which are utilized to determine the atom's presence. A monochromatic light falls on the sample's specimen in this procedure. The vibrational frequency of the chemical link between the atoms interacts with the light. The light with a wavelength similar to the bond is absorbed by the atoms, and the remaining light is sent to the sensors in the operation chamber, allowing the absorbed frequency to be visualized by subtracting the received wavelength from the source. Raman shifts are mostly determined by wave number (cm^{-1}). There are three levels of energy emission as a result of light absorption. When an infrared photon is absorbed by a substance, the material's vibrating bond can emit or scatter photons of the same wavelength. Rayleigh scattering is the name for this sort of scattering. There is a chance of scattering. Anti-stokes scattering is the scattering of photons with higher energy than those absorbed. Stokes scattering is the name given to the scattering of photons. Possess a lower energy than the absorbed photon

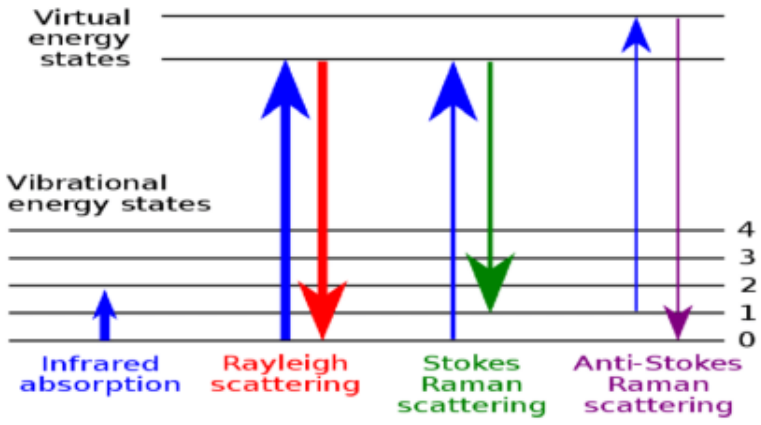

Figure 3-5 Energy level diagram

3.6 Electrochemical analysis

Electroanalytical methods involve the analysis of analyte by measurement of current and voltage in the electrochemical cell. Three basic types are potentiometry, coulometry and voltammetry. Potentiometry involves the measurement of electrode potential.

Coulometry involves the measurement of current as a function of time and volumetric analysis is a measure of current as a function of voltage.

In most cases, measurements are carried out in an electrochemical cell with three different types of electrodes, as illustrated in the diagram.

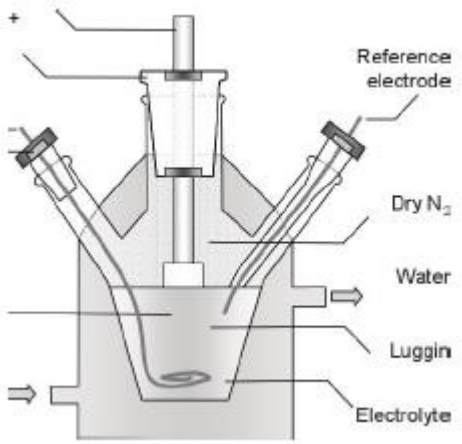

Figure 3-6 Schematic of electrochemical workstation electrode assembly

As a reference electrode, Ag/AgCl, Hg/HgO and standard hydrogen electrode (SHE) are commonly used. Other electrodes' potential is assessed in relation to the reference electrode. The electrical circuit is completed by the counter electrode. It permits electrons to pass from the working electrode to the counter electrode while measuring current. For analysis, platinum wire, gold, or carbon-based counter electrodes are commonly used. The counter electrode, also known as the auxiliary electrode, is a current-conducting electrode used in electrochemical cells to complete the circuit. Because the reference electrode has a fixed potential value, any change in the cell (redox process) is attributed to the other two electrodes. To function as a counter electrode, an electrode must meet the following requirements:

- This electrode's reaction product should not react with the working electrode.
- It should not dissolve in the electrochemical cell's medium (electrolyte).
- Its electrode area must be bigger than the working electrode's so that the limiting current is not affected.

A platinum wire and, in many cases, carbon electrodes make up the counter electrodes. A platinum sheet was employed as a counter electrode in this study.

In the working window of analysis, the working electrodes are electrochemically inert. Over the working electrode, interest reactions occur. In electrochemical analysis, the glassy carbon electrode (GCE) is the most often employed working electrode.

Figure 3-7 Electrochemical workstation in SCME

3.6.1 Cyclic Voltammetry (CV)

The CV is the simplest method for measuring the electrochemical behavior of a material on a laboratory scale. CV can be used to analyze redox processes that occur at the electrode/electrolyte contact. Three electrodes make up the CV system. The potential is charged on the WE and RE in CV, and the output current response between the working and counter electrodes is recorded. The resultant current(I) of WE vs. the potential is represented by the CV curve (V). Between the WE and the RE, potential is applied. Platinum makes up most of the counter electrode. The electrolyte's function is to provide ions. The conductivity of the electrolyte must be high. Different materials react differently in supercapacitors. During forward and reverse scans, the EDLC produces a rectangular curve, whereas the pseudo capacitor produces an oxidation and reduction hump, indicating redox processes, as seen in Fig.

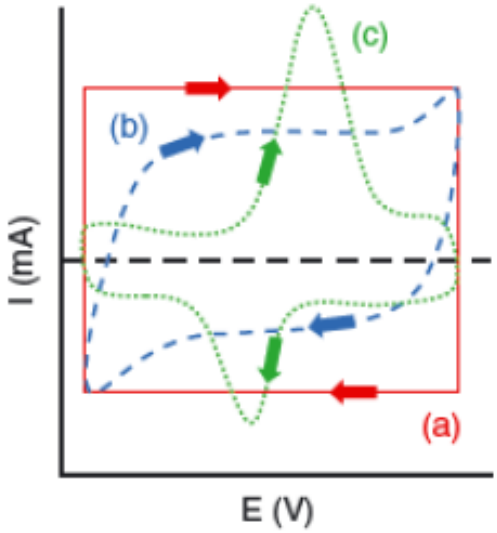

Figure 3-8 Figure 3-15 CV curves of (a) Ideal capacitor (b)EDLC (c)Pseudo capacitor [24]

3.6.2 Galvanostatic Charge-Discharge (GCD)

The most frequent way for testing the charging and discharging of supercapacitors and batteries is to use GCD. GCD is a technique for measuring potential over time with a constant current. EDLC and Pseudo capacitor have various GCD curves, similar to CV. The GCD curve of EDLC materials is linear, however the Pseudo capacitor curve is not long, indicating that a redox reaction has occurred, as illustrated in fig. It is a reliable method for evaluating materials electrochemically. The GCD method differs from cyclic voltammetry in that the current is controlled while the voltage is measured. The GCD method is one of the most widely used electrochemical techniques, with the ability to scale up from lab to industrial proportions. This technique is also known as chronopotentiometry, and it provides information on the following parameters:

- Capacitance
- Resistance
- Stability

GCD works on the idea of applying a current pulse to the working electrode WE and measuring the resulting potential as a function of time. In a GCD test, the voltage fluctuation is provided by the equation below.

V(t) denotes a variable voltage as a function of time, iR denotes internal resistance, C denotes capacitance, and I denotes current. The slope of the GCD curve can be used to compute capacitance C, as shown in equation.

Because V(t) does not vary linearly in a V(t) curve profile in the case of a pseudo capacitor, the capacitance can be estimated by integrating current across the charge or discharge time as indicated in equation.

$$\mathbf{C}=\boldsymbol{I\Delta t\Delta V}$$

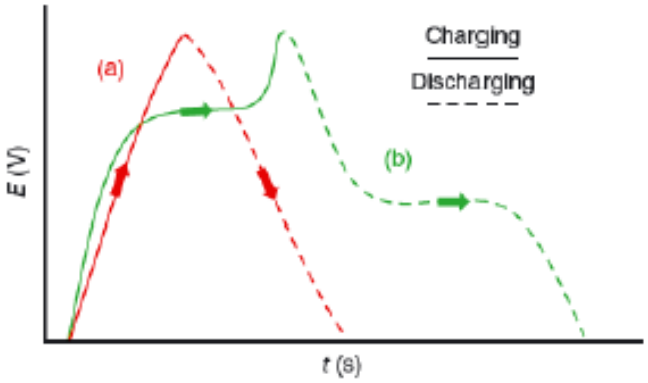

Figure 3-9 GCD of (a) EDLC curve (b) Pseudo capacitor curve [26]

3.6.3 Cyclic Stability

One of the most important characteristics of energy storage devices is cyclic stability. Multiple charge-discharge cycles are used to test the cyclic performance of supercapacitors. On a lab scale, charge-discharge cycles ranging from 500 to 10,000 were used to test the material's capacitance retention.

3.6.3 Electrochemical Impedance Spectroscopy

This is a widely used approach for material impedance analysis. It is a sensitive approach that provides information on the electrochemical reaction at the contact, the reaction mechanism, intermediates, and the material's composition. Sensing, corrosion, fuel, capacitors, and resistance research are some of the applications[64-67]

3.6.3.1 Working Principle

As shown in figure 44, the response of the analyte is recorded after the application of alternating current signals (a). EIS is carried out at various intervals. The only disadvantage of EIS is the low selectivity of input parameters [68, 69] It is a sensitive technique that can be employed for analyte detection. The EIS is carried out at various intervals. The EIS curve is made up of two sections: a real axis and a semicircle. The shape of the curve created by EIS material testing is determined by the material's characteristics. For optimal systems, the true axis should be vertical and the semicircle should be smaller for ideal capacitive materials. The Nyquist plot is used to determine the value of resistances. To analyze the system's impedance, an appropriate circuit is chosen to perform the z-fitting.

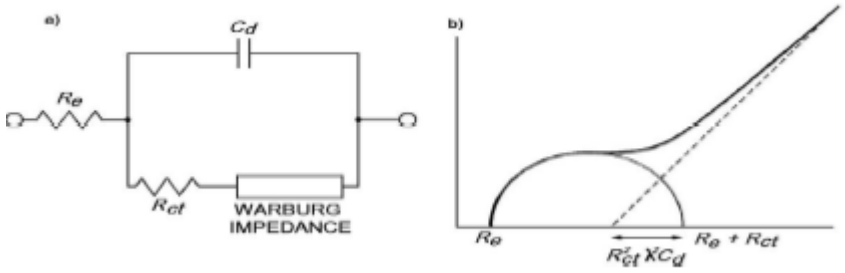

Figure 3-10 EIS (a) Equivalent circuit diagram (b)Nyquist plot

Here, Re denotes the solution resistance, which is the series resistance at the working electrode-electrolyte interface, Rct denotes the charge transfer resistance or polarization resistance, and Cd denotes the double layer capacitance, which is the interface capacitance between electrode and electrolyte, as well as the wanburg impedance, which is dependent on reactant diffusion.

Chapter 4

Results and Discussions

4.1 Analysis of Phase Structure

Powdered X-ray diffraction machine step scan of 0.04o and scan rate of 1.00 s was used to investigate the structural properties of the produced material.

4.1.1 XRD analysis of FeSe

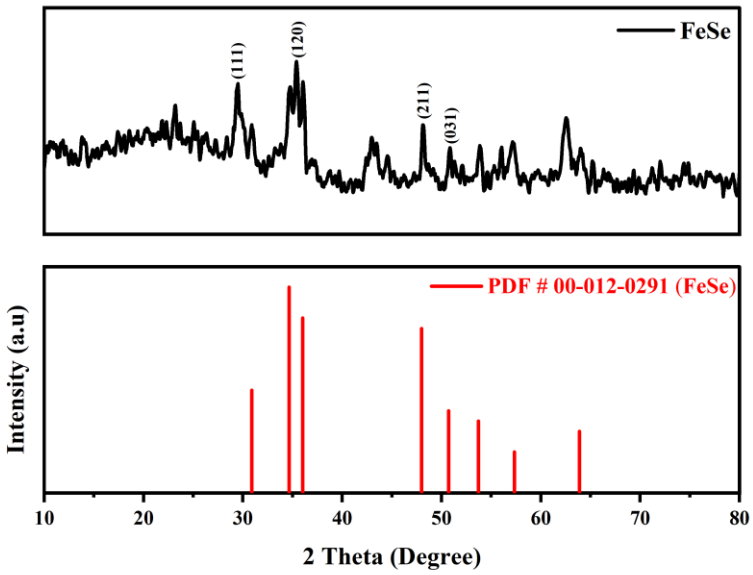

Figure 4-1 XRD analysis of FeSe

The structural and compositional analysis of synthesized iron selenide was studied using XRD. The XRD data support the formation of a homogeneous orthorhombic structure of FeSe, which is in perfect agreement with JCPDS Card no. 00-012-0291. In the XRD pattern of FeSe, there are no peaks of any kind of impurity. The highest x-ray diffraction was obtained along the crystal plane (1 2 0), with a diffraction angle of $2\theta = 36.024°$. The additional peaks, which can be found at 34.645°,36.024°, 47.993°, and 53.715°, correspond to the planes (1 1 1), (1 2 0), (2 1 1), and (0 3 1), respectively. The crystallite size of FeSe was calculated by Scherrer formula

$$D=0.9\lambda/(\beta\cos\theta)$$

Where λ is the wavelength, B is the FWHM, and θ is the angle of the diffracted peak. The crystallite size for the corresponding planes is calculated as 28.2 nm, 56.5 nm, 29.4 nm, 22.6 nm.

4.1.2 XRD analysis of ZnSe

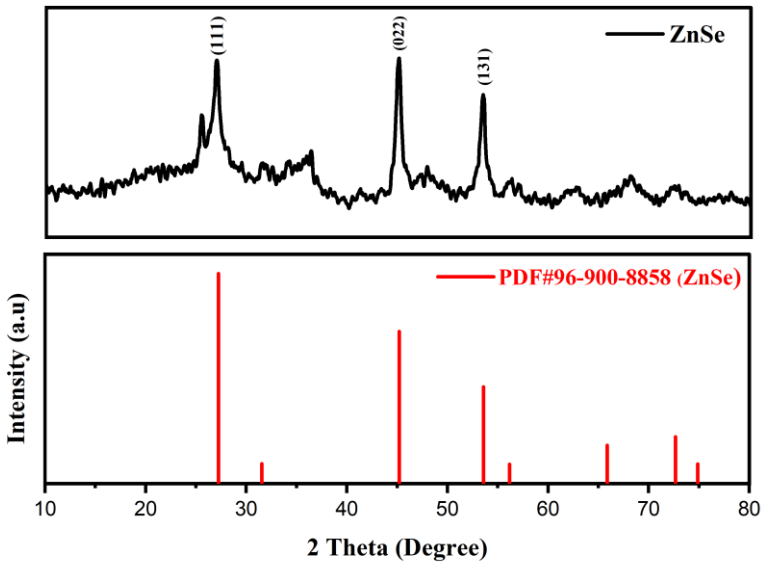

Figure 4-2 XRD analysis of ZnSe

The structural and compositional analysis of synthesized zinc selenide was studied using XRD. The XRD data support the formation of a homogeneous cubic structure of ZnSe, which is in perfect agreement with JCPDS Card no. 96-900-8858. In the XRD pattern of ZnSe, there are no peaks of any kind of impurity. The highest x-ray diffraction was obtained along the crystal plane (1 1 1), with a diffraction angle of 2θ = 27.231°. The additional peaks, which can be found at 27.231°, 45.213° and 53.582°, correspond to the planes (1 1 1), (0 2 2) and (1 3 1), respectively. The crystallite size of ZnSe was calculated by Scherrer formula

$$D=0.9\lambda/(\beta\cos\theta)$$

Where λ is the wavelength, B is the FWHM, and θ is the angle of the diffracted peak. The crystallite size for the corresponding planes are calculated as 20.7 nm, 43.7 nm, 22.6 nm.

4.1.3 XRD analysis of FeZnSe

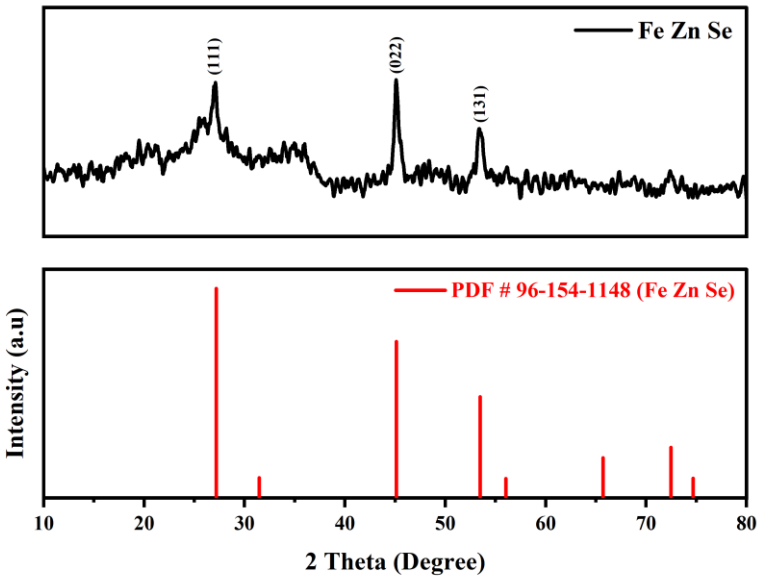

Figure 4-3 XRD analysis of FeZnSe

The structural and compositional analysis of synthesized Iron Zinc Selenide was studied using XRD. The XRD data support the formation of a homogeneous cubic structure of Fe Zn Se, which is in perfect agreement with JCPDS Card no. 96-154-1148. In the XRD pattern of Fe Zn Se, there are no peaks of any kind of impurity. The highest x-ray diffraction was obtained along the crystal plane (1 1 1), with a diffraction angle of 2θ = 27.17°. The additional peaks, which can be found at 27.17°, 45.11° and 53.46°, correspond to the planes (1 1 1), (0 2 2) and (1 3 1), respectively. The 1:2 ratio of both metal sulphates resulted in a stoichiometric pure phase of FeZnSe, according to the results. This analysis shows that zinc sulphate has a higher retention ability than iron sulphate, resulting in a higher amount of zinc when compared to iron. The crystallite size of FeZnSe was calculated by Scherrer formula

$$D=0.9\lambda/(\beta\cos\theta)$$

Where λ is the wavelength, B is the FWHM, and θ is the angle of the diffracted peak. The crystallite size for the corresponding planes are calculated as 20.7 nm, 21.8 nm and 22.5 nm.

4.2 Micro-Structural Analysis

4.2.1 SEM

The microstructural examination of synthesized material was studied using SEM. After that, the powdered sample was used for the analysis. An ion sputtering device was used to cover the sample with gold to make it conduct. The SEM images confirmed the formation of binary metal selenide nanosheets randomly.

4.2.2 Iron Selenide (FeSe)

A high-resolution SEM picture of FeSe is shown in Figure (a) shows SEM image of precursor nanosheets before selenization. Figure (b) SEM image shows FeSe after selenization. It was observed that our FeSe consisted of nanosheets arranged in a random order, with multiple selenide nanoparticles nucleating heterogeneously over the precursor nanosheets.

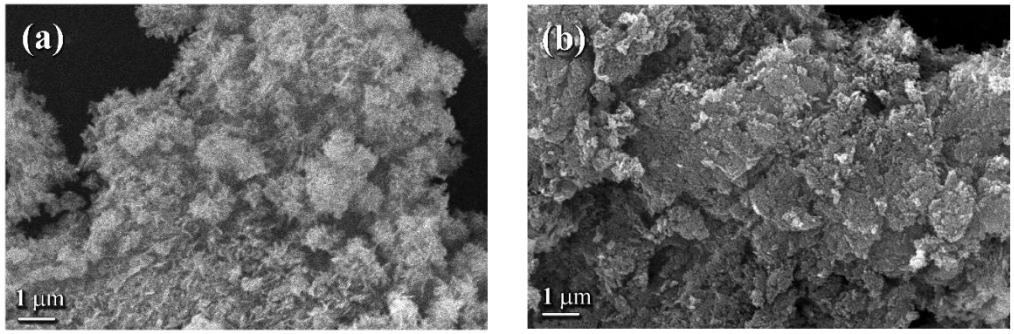

Figure 4-4 (a) Fe precursor nanosheets (b) FeSe nanosheets after selenization

4.2.3 Zinc Selenide (ZnSe)

A high-resolution SEM picture of ZnSe is shown in Figure . Figure (a, b) shows SEM image of precursor nanosheets before selenization. Figure (c,d) SEM image shows ZnSe after selenization. It was observed that our ZnSe consisted of nanosheets arranged in a random order, with multiple selenide nanoparticles nucleating heterogeneously over the precursor nanosheets. This arrangement of nanosheets help in movement of charges

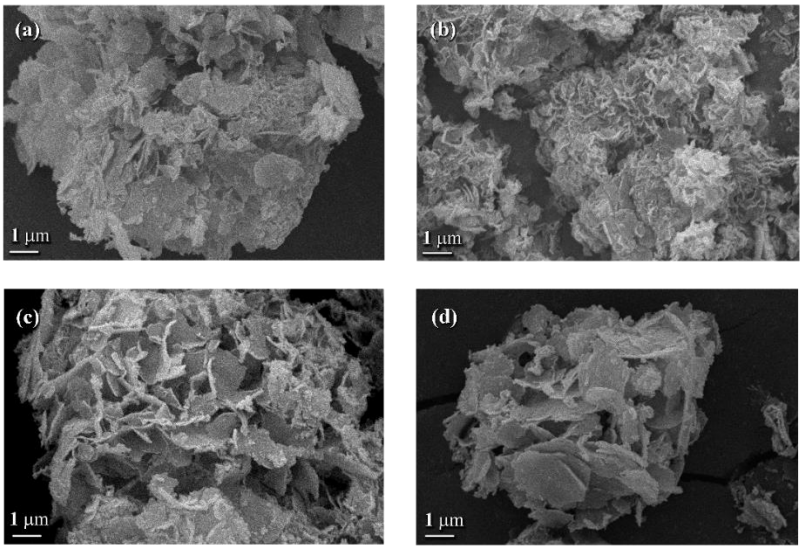

Figure 4-5 (a,b) Fe precursor nanosheets (c,d) FeSe nanosheets after Selenization

4.2.4 Iron Zinc Selenide (FeZnSe)

A high-resolution SEM picture of FeZnSe is shown in Figure . Figure (a,b) shows SEM image of precursor nanosheets before selenization. Figure (c,d) SEM image shows FeZnSe after selenization. It was observed that our FeZnSe consisted of nanosheets, with multiple selenide nanoparticles nucleating heterogeneously over the precursor nanosheets. The synergetic chemistry of iron, zinc, and selenide allows for this type of atom arrangement to form this structure.

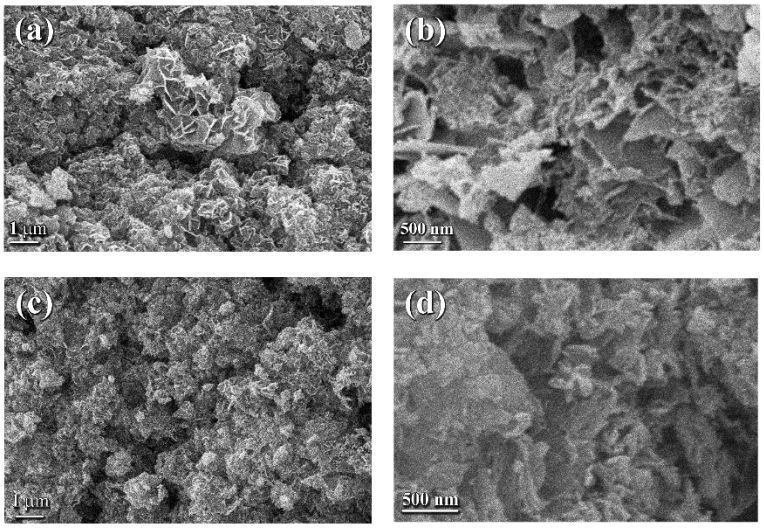

Figure 4-6 (a,b) FeZn precursor nanosheets (c,d) FeZnSe nanosheets after Selenization

4.4 EDX

4.4.1 Iron Selenide

EDX was performed for FeSe by the EDS detector. The analysis of EDX confirmed the presence of required elements iron and selenium. Iron and selenium are present in 35.6 and 20.8 by atomic weight percent. EDS spectrum shows sharp peaks of Iron and Selenium.

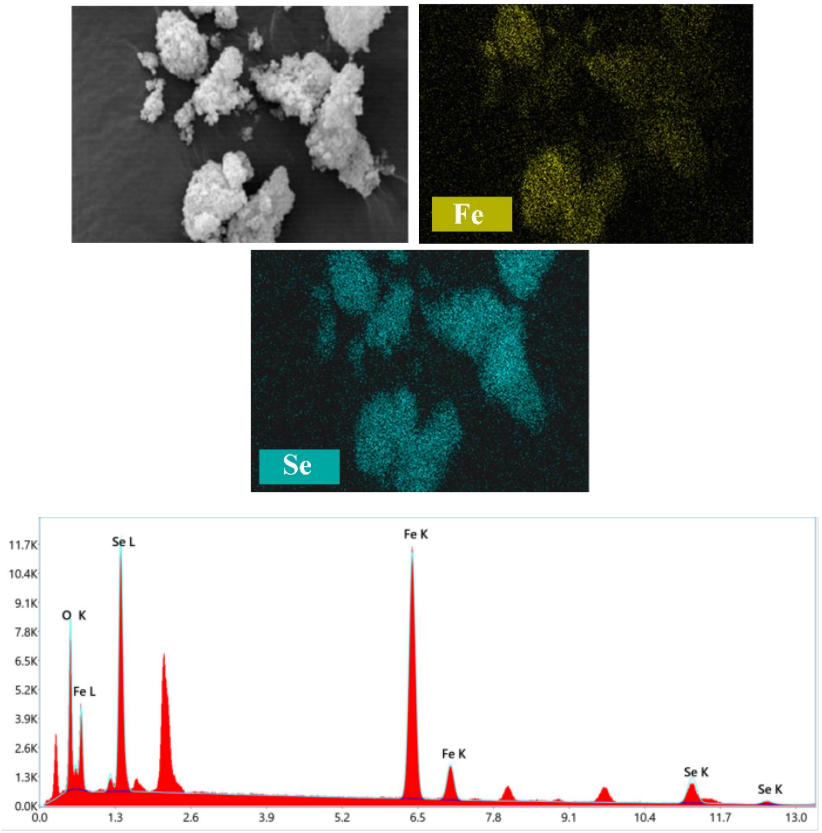

Figure 4-7 EDX of FeSe

Table 4-1 EDX of Iron Selenide

Element	Weight %	Atomic %
Fe	46.0	35.6
Se	37.9	20.8

4.4.2 Zinc Selenide

EDX was performed for ZnSe by the EDS detector. The analysis of EDX confirmed the presence of required elements Zinc and selenide. Zinc and selenium are present in 42.5 and 39.3 by atomic weight percent. EDS spectrum shows sharp peaks of Zinc and Selenium.

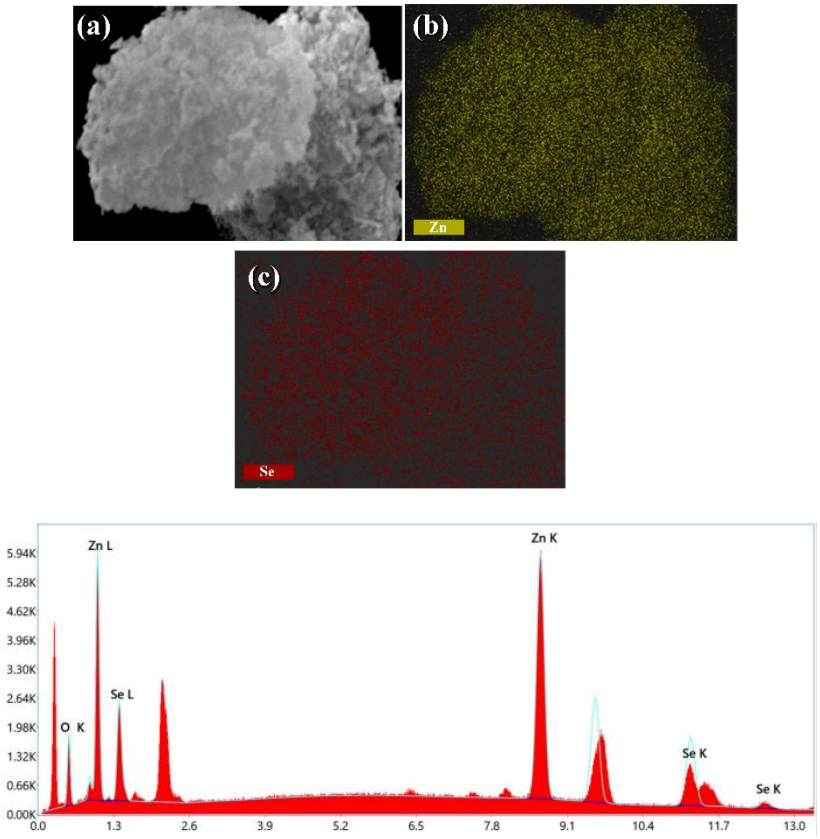

Figure 4-8 EDX of ZnSe

Table 4-2 EDX of Zinc Selenide

Element	Weight %	Atomic %
Zn	45.1	42.5
Se	50.2	39.3

4.4.3 Iron Zinc Selenide

EDX was performed for FeZnSe by the EDS detector. The analysis of EDX confirmed the presence of required elements Iron, Zinc and selenide. Iron, Zinc and selenium are present in 15.8, 25.5 and 11.0 by atomic weight percent. EDS spectrum shows sharp peaks of Iron, Zinc and Selenium. From EDS measurements we get **$Fe_{0.38}Zn_{0.62}Se$.**

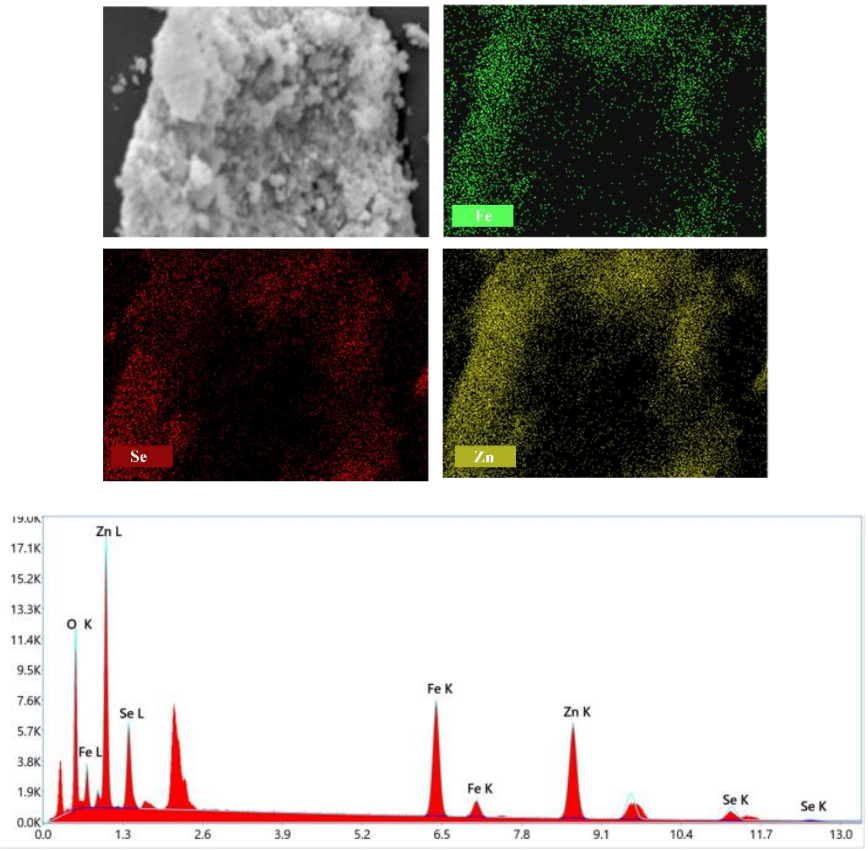

Figure 4-9 EDX of FeZnSe

Table 4-3 EDX of Binary Fe Zn Se

Element	Weight %	Atomic %
Fe	21.1	15.8
Zn	39.9	25.5
Se	20.7	11.0

4.5 TEM of FeZnSe

The microstructural analysis of FeZnSe was studied further using TEM. The TEM examination of FeZnSe at a depth of focus of 200 nm is shown in Figure (a). A TEM image of FeZnSe at a depth of focus of 0.5 um is shown in Figures (b) and (c). The images confirmed that the FeZnSe material is made up of nanosheets made up of small particles that are homogeneous in size.

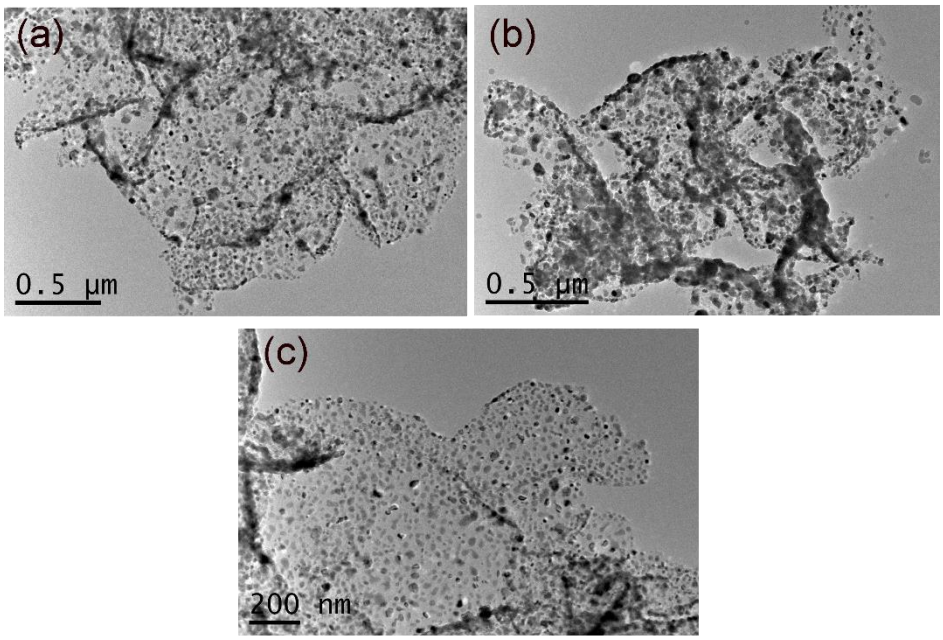

Figure 4-10 TEM of FeZnSe

4.6 BET

N2 absorption was performed to do the analysis of the specific surface area of the prepared samples. Electrochemical performance of the sample is in linear state with the surface area. The prepared FZSe nanosheet BET surface area is 44.6396 m^2/g. The average pore width of the prepared sample is 17.2 nm. The increased specific area of FZSe enables efficient electrolyte transfer and an increase in reactive sites, resulting in enhanced electrochemical performance. The surface area of FeSe and ZnSe are 57.2 m^2/g and 29.2 m^2/g.

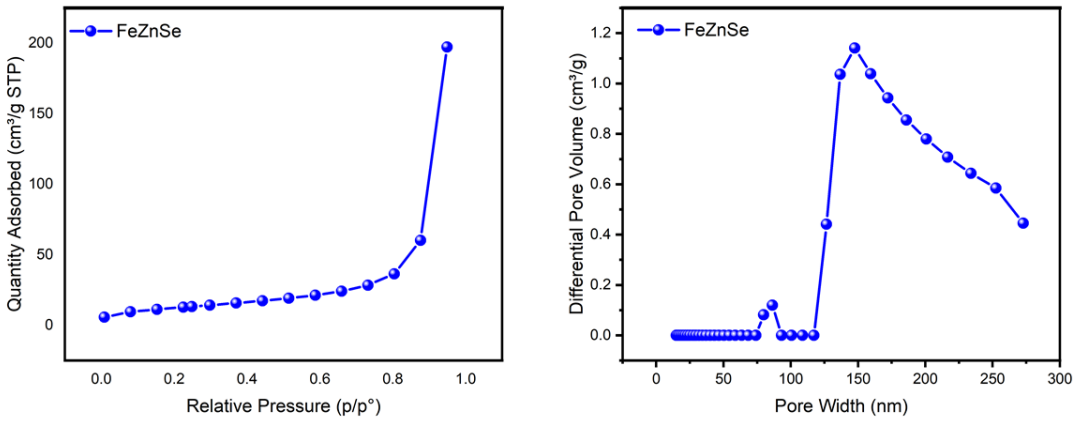

Figure 4-11 BET of FeZnSe

4.7 Electrochemical characterizations

4.7.1 Cyclic Voltammetry (CV)

At varied scan speeds, it was used to visualize the capacitive response type of FeSe, ZnSe, and FeZnSe.

4.7.2 Iron Selenide (FeSe)

The CV curves for iron selenide at 10 mVs^{-1}, 20 mVs^{-1}, 30 mVs^{-1}, 50 mVs^{-1}, 80 mVs^{-1}, and 100 mVs^{-1} are shown in Figure. The CV was carried out between -0.2 V and 0.5 V in potential range. The pseudocapacitive behavior of FeSe was shown by the non-rectangular graph of cyclic voltammogram. With the scan rate, the current value in response to the applied potential difference increases. The CV curves of FeSe showed redox peaks.

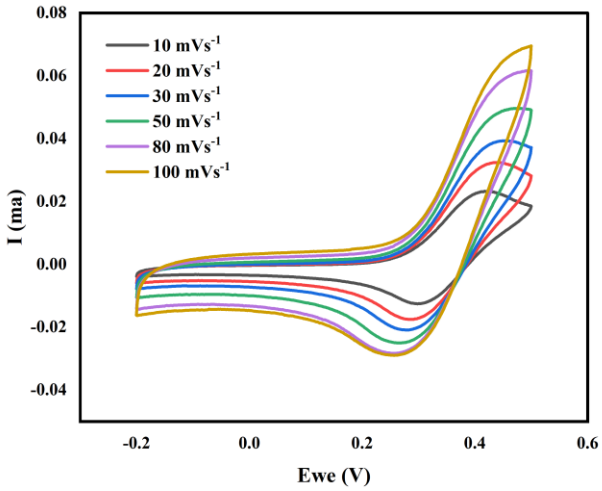

Figure 4-12 CV graph of FeSe

4.7.3 Zinc Selenide (ZnSe)

The CV curves for zinc selenide at 10 mVs^{-1}, 30 mVs-1, 50 mVs^{-1}, 80 mVs^{-1}, and 100 $mVs^{-1}$are shown in Figure. The CV was carried out between -0.2 V and 0.8 V in potential range. The pseudocapacitive behavior of ZnSe was shown by the non-rectangular graph of cyclic voltammogram. With the scan rate, the current value in response to the applied potential difference increases. The CV curves of ZnSe showed redox peaks.

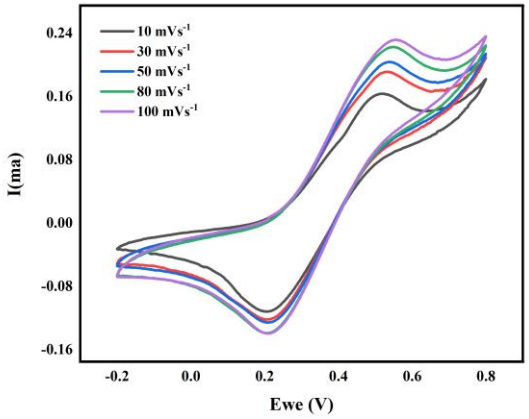

Figure 4-13 CV graph of ZnSe

4.7.4 Iron Zinc Selenide (FeZnSe)

The CV curves for iron zinc selenide at 10 mVs^{-1}, 20 mVs^{-1}, 30 mVs^{-1}, 50 mVs^{-1}, 80 mVs^{-1}, and 100 $mVs^{-1}$are shown in Figure. The CV was carried out between -0.2 V and 0.5 V in potential range. The pseudocapacitive behavior of FeZnSe was shown by the non-rectangular graph of cyclic voltammogram. With the scan rate, the current value in response to the applied potential difference increases. The CV curves of FeZnSe showed redox peaks.

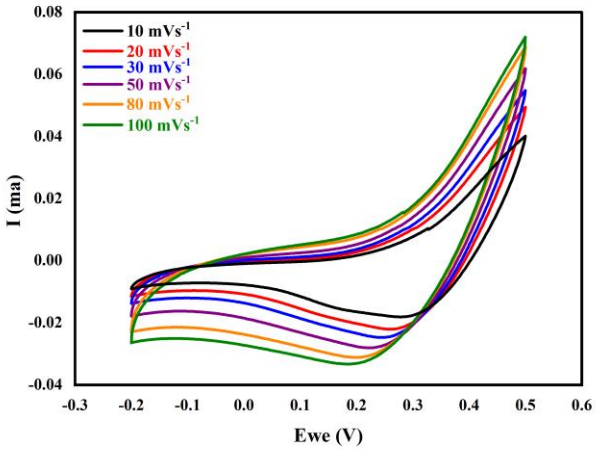

Figure 4-14 CV graph of FeZnSe

4.7.5 Galvanostatic charge and discharge (GCD)

For the study of charge storage capacity of materials, the galvanostatic charge and discharge technique is quite effective. The GCD was used to determine how long it takes for the material to charge and how long it can maintain that charge. Calculating specific capacitance using GCD is the most precise method. Capacitance is calculated by

$$\mathbf{Cs= \mathit{I}*\mathit{t}/m*\Delta V}$$

Here, "t" stands for discharge time, "I" for current density, and "m" for mass of active material, while "V" stands for the voltage drop during discharge.

4.7.5 Iron Selenide

We used GCD to investigate the capacitive properties of FeSe after visualizing the capacitive nature of the material using a cyclic voltammetry curve. As shown in fig. , we performed the GCD at various current densities to explore the ability of FeSe to

sustain charge in greater detail. On a current density of 1 Ag^{-1}, the maximum time for charge maintaining was measured. Because of the low capacitance, the charge sustain time reduced when the current density was raised. The capacitance calculated for FeSe was 395 F/g, 285 F/g,186 F/g, 133 F/g and 91 F/g.

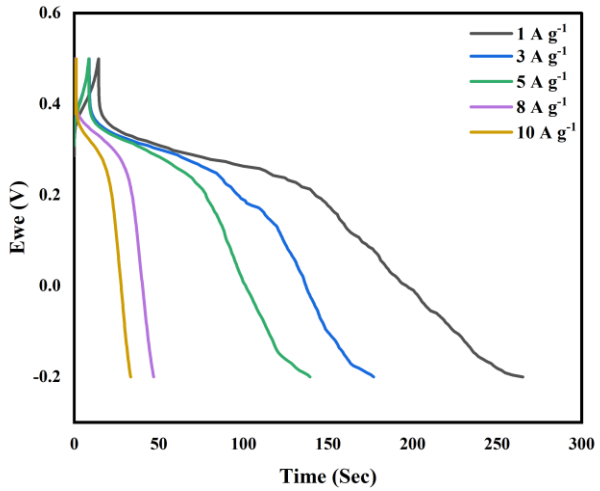

Figure 4-15 GCD of FeSe

4.7.6 Zinc Selenide

We used GCD to investigate the capacitive properties of ZnSe after visualizing the capacitive nature of the material using a cyclic voltammetry curve. As shown in fig. , we performed the GCD at various current densities to explore the ability of ZnSe to sustain charge in greater detail. On a current density of 1 Ag^{-1}, the maximum time for charge maintaining was measured. Because of the low capacitance, the charge sustain time reduced when the current density was raised. The capacitance calculated for ZnSe was 358.2 F/g, 329.1 F/g, 289.09 F/g.

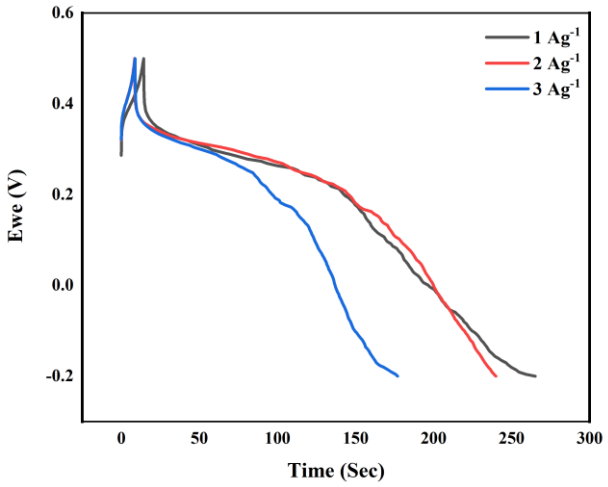

Figure 4-16 GCD of ZnSe

4.7.7 Iron Zinc Selenide

We used GCD to investigate the capacitive properties of FeZnSe after visualizing the capacitive nature of the material using a cyclic voltammetry curve. As shown in fig. , we performed the GCD at various current densities to explore the ability of FeZnSe to sustain charge in greater detail. On a current density of 0.5 Ag^{-1}, the maximum time for charge maintaining was measured. Because of the low capacitance, the charge sustain time reduced when the current density was raised. The capacitance calculated for FeZnSe was 1140 F/g, 537 F/g, 285 F/g, 114 F/g, 57 F/g. The GCD curves illustrate the faradaic behavior of all the different materials, as all of the curves show a nonlinear response, indicating that the faradaic reaction occurs and charge storage is due to oxidation and reduction. The curves clearly show that Binary selenide FeZnSe has a longer discharge time than other mono-metals.

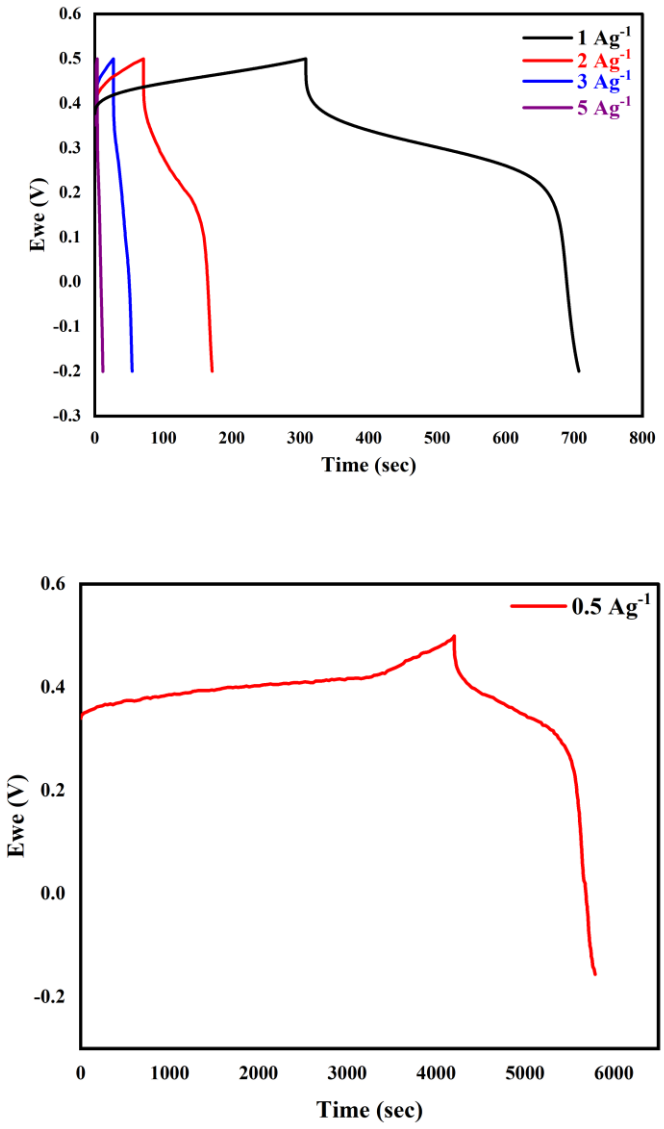

Figure 4-17 GCD of FeZnSe

Following are some of the graphs of (a) specific capacitance vs current density (b) specific capacitance vs sample at 1 Ag^{-1}

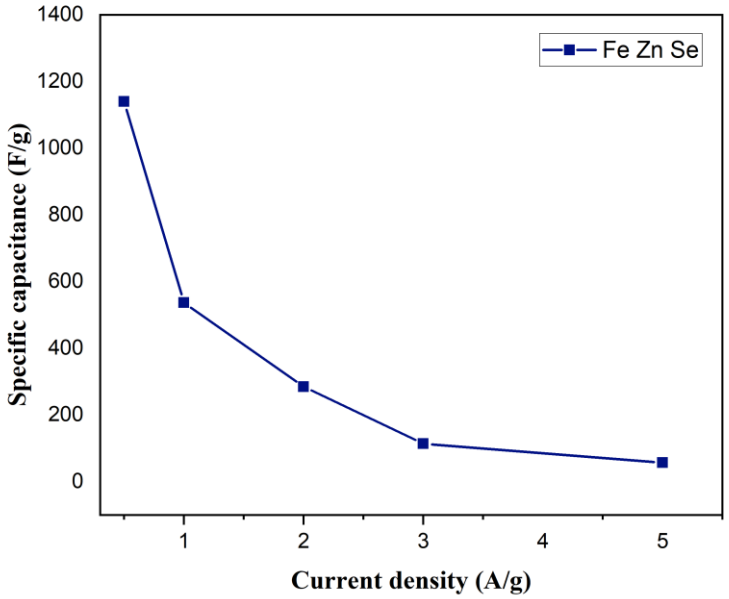

Figure 4-18 Specific capacitance vs current density

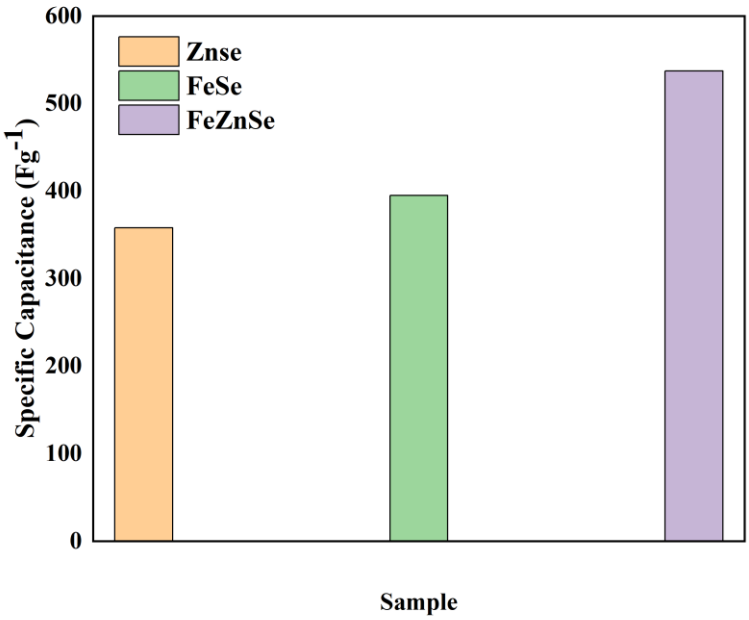

Figure 4-19 Specific capacitance vs sample

4.7.8 Charge stability

Charge stability is a key aspect for electrode materials used in supercapacitors from a practical standpoint. To investigate the stability of FeZnSe in terms of maintaining charge for a long period of time. At a current density of 5 Ag^{-1}, we used the GCD approach for approximately 5000 cycles. FeZnSe exhibited exceptional charge stability with a coulombic efficiency of 100% and capacitance retention of 75% approximately 5000 cycles.

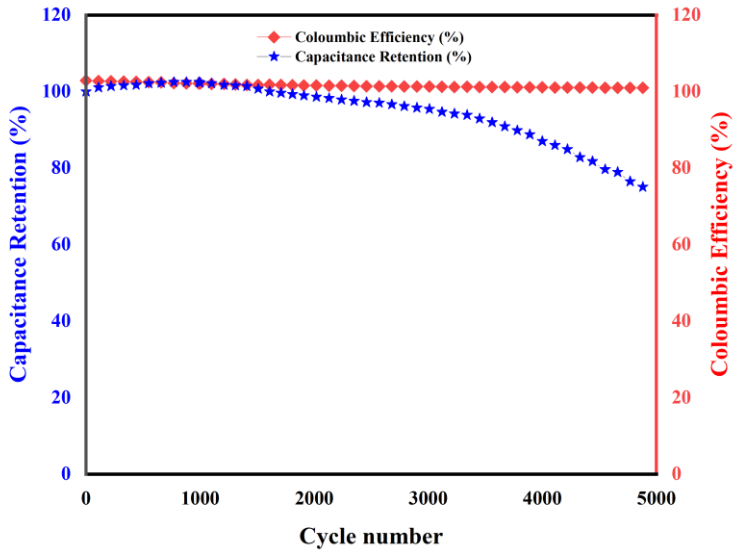

Figure 4-20 coulombic efficiency vs capacitance retention

Table 4-4 A brief comparison of electrochemical properties of FeSe, ZnSe,FeZnSe

Sample	Current Density (Ag^{-1})	Specific Capacitance (Fg^{-1})
FeSe	1	395
	3	285
	5	186
	8	133
	10	91
ZnSe	1	358.2
	2	329.1
	3	289.09
FeZnSe	0.5	1140
	1	537
	2	285
	3	114
	5	57

4.7.9 Electrochemical Impedance Spectroscopy (EIS)

It was carried out to determine the system's resistances. The EIS graph is divided into two parts: a real axis and a hemicircle. The internal resistances of the system, such as resistance between the electrode material and the electrolyte, electrolyte ionic resistance, and electrode resistance, are shown on the graph's real axis. The diffusion coefficient of electrolyte with electrode material is also studied using the real axis. The real axis of ideally capacitive materials should be vertical. The charge transfer resistance of the electrode material is shown in the semicircle area. The semicircle's diameter is determined by the charge transfer resistance. The larger the semicircle, the greater the charge transfer resistance. When compared to Binary Iron Zinc Selenide, the semicircle for Iron Selenide and Zinc Selenide is larger, indicating a higher charge transfer resistance. Due to its random ordered morphology of nanosheets, the charge transfer resistance of Iron Selenide and Zinc Selenide is higher, with charge transfer resistance of

167 ohms and 100 ohms, respectively. In the case of Binary Iron Zinc Selenide, the nanosheets are arranged in a sequence and diffusion of the electrolyte's efficient ions making charge transfer easier and lowering charge transfer resistance as compared to mono-metals. Binary Iron Zinc Selenide has a charge transfer resistance of 19.1 ohm. Binary FeZnSe low resistive value shows the diffusion of the electrolyte's efficient ions during the electrochemical process as well as capacitance increase due to strong conductivity, unique architecture with a large surface area and good performance, especially in terms of high rate capability and long-term stability.

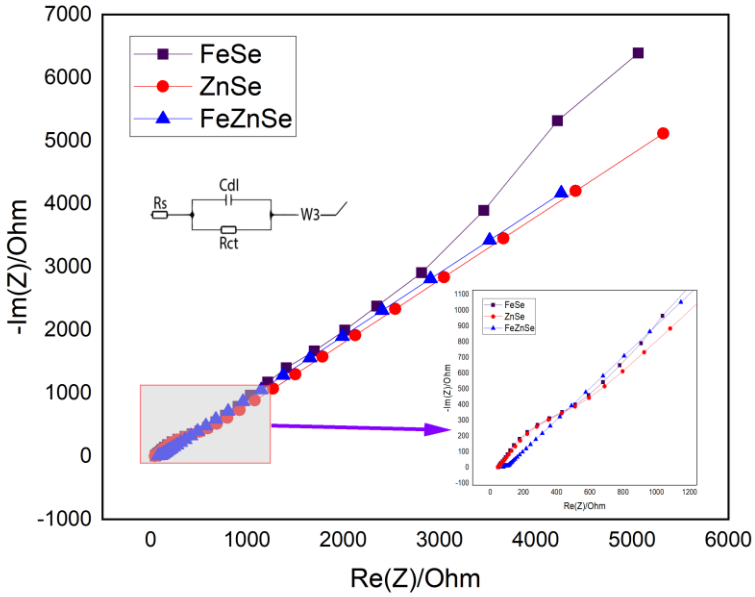

Figure 4-21 EIS of Fese, ZnSe, FeZnSe

4.7.10 Performance of Asymmetric device

The growth of supercapacitors with both types of capacitive nature EDLC and pseudo made it feasible to create an energy storage device with high power density and higher energy density. The asymmetric type of supercapacitor is made up of two electrodes with opposing capacitive material properties, such as one that exhibits EDLC behavior and the other that exhibits a faradic type reaction for charge storage. Two

electrode systems were used to conduct electrochemical testing on an asymmetric supercapacitor. The FeZnSe positive electrode and activated carbon negative electrode are submerged in 1 M Na2SO4 electrolyte in an electrochemical cell. The charge balance between the positive and negative electrodes had a significant impact on the performance of asymmetric supercapacitors, as shown by the equation:

$$m+/m- = c-\times\Delta V-/c+\times\Delta V+$$

Where m denotes the electrode mass in grams, C is the specific capacitance in Fg^{-1}, and V denotes the potential window. All of the tests were carried out within a broad operating range of 0 to 1.5 V.

4.7.11 Cyclic Voltammetry (CV)

Both types of electrochemical reactions (Faradic ion exchange and electrostatic charge accumulation on the surface) were implicated in the CV curve for asymmetric devices. The current passing through the device was increased as the scan rate was increased. The shape of the CV curve changes as the potential window is increased, which is consistent with the charge storage process of pseudo capacitors.

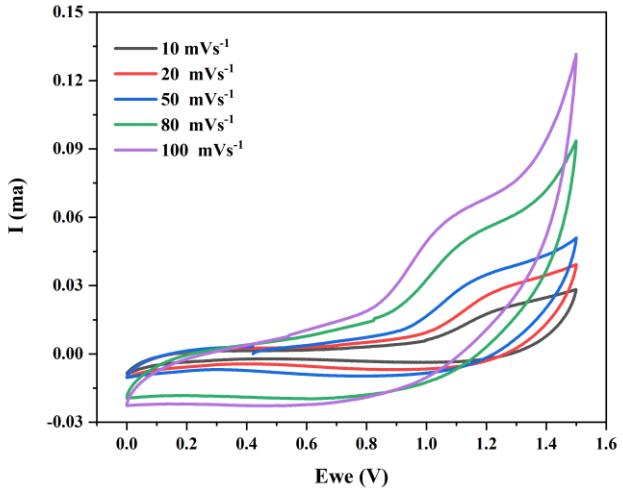

Figure 4-22 CV Graph of Asymmetric device

4.7.11 Galvanostatic charge and discharge (GCD)

After visualizing the nature of the electrochemical reactions involved in the asymmetric device's energy storage, we used GCD to see how long it took to charge and

discharge the asymmetric device at different current densities. The GCD curves for FeZnSe/AC asymmetric device at various current densities are shown in Figure. The device's discharge time was lowered when the current density was increased, as can be observed. At current densities of 0.4 Ag^{-1}, 0.5 Ag^{-1}, 0.8 Ag^{-1}, 1 Ag^{-1}, and 1.5 Ag^{-1}, the specific capacitance of FeZnSe/AC asymmetric device was 120 Fg^{-1}, 59.3 Fg^{-1}, 48 Fg^{-1}, 26.5 Fg^{-1}, and 11.26 Fg^{-1}, respectively.

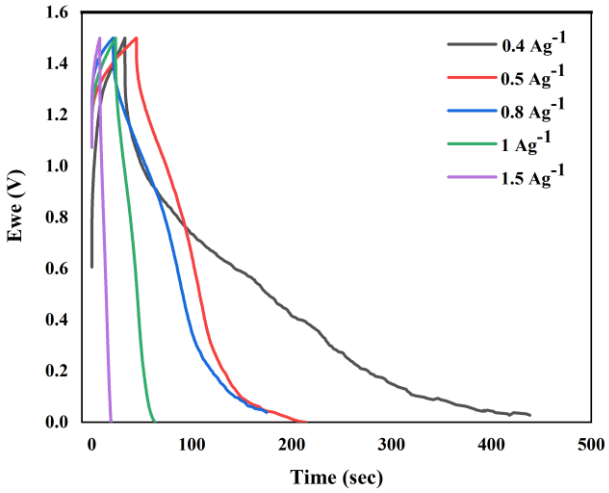

Figure 4-23 GCD Graph of Asymmetric device

Further we have a graphical representation of Specific capacitance vs current density.

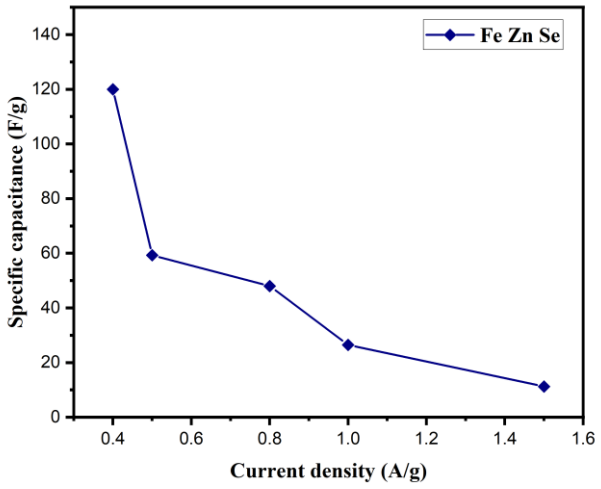

Figure 4-24 Specific capacitance vs current density

4.7.12 Charge Stability

With high specific capacitance, cyclic stability is the most important factor for practical devices. We ran 7000 GCD cycles at 8 Ag^{-1} current density to evaluate cyclic stability. Figure depicts a comparison of the asymmetric device's coulombic efficiency and capacitance retention. It exhibited exceptional charge stability with a coulombic efficiency of 93% and capacitance retention of 83.5 for approximately 7000 cycles.

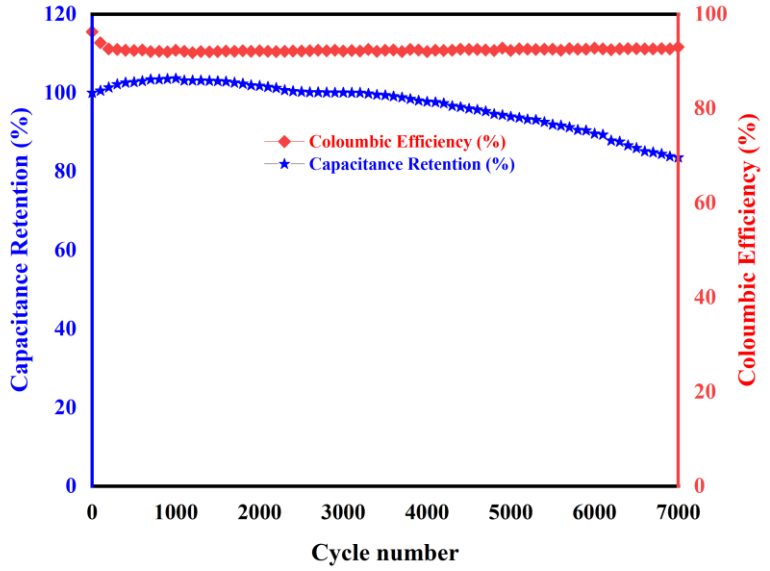

Figure 4-25 coulombic efficiency vs capacitance retention

4.7.13 Energy density vs Power density

The Ragone plot is by far the most effective tool for comparing materials' ability to store energy [60]. Figure 1 shows the corresponding Ragone plot for FeZnSe comparison with literature. The fundamental disadvantage of supercapacitors in comparison to batteries is their low power density. The use of FeZnSe as an electrode material in supercapacitors can help to alleviate this shortcoming. FeZnSe can be used to achieve both high energy and high-power density. At a current density of 0.4 Ag^{-1}, FeZnSe exhibits a higher energy density of 50 $Whkg^{-1}$ and a power density of up to 400 Wkg^{-1}, and additional studies revealed that a high power density of 1440 Wkg^{-1} with an energy density of 10.6 $Whkg^{-1}$ can be attained at a current density of 1 Ag^{-1}.

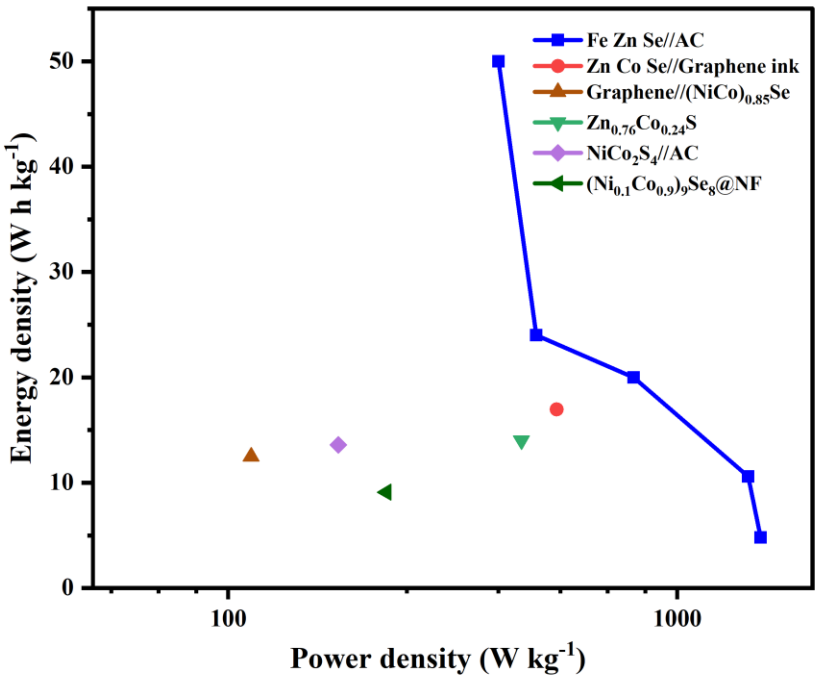

Figure 4-26 Ragone Plot

References

[1] Solar energy conversion. Dalton Transactions, (2009)(45): p. 9951-9951.

[2] Usman, M., et al., Facile synthesis of ironnickelcobalt ternary oxide (FNCO) mesoporous nanowires as electrode material for supercapacitor application. Journal of Materiomics, (2022). **8**(1): p. 221-228.

[3] Glassmeyer, S.T., et al., Nationwide reconnaissance of contaminants of emerging concern in source and treated drinking waters of the United States. Science of The Total Environment, (2017). **581-582**: p. 909-922.

[4] Balat, M. and H. Balat, Recent trends in global production and utilization of bio-ethanol fuel. Applied Energy, (2009). **86**(11): p. 2273-2282.

[5] Zhu, K., et al., Fast synthesis of uniform mesoporous titania submicrospheres with high tap densities for high-volumetric performance Li-ion batteries. Science China Materials, (2017). **60**(4): p. 304-314.

[6] Miller, E.E., Y. Hua, and F.H. Tezel, Materials for energy storage: Review of electrode materials and methods of increasing capacitance for supercapacitors. Journal of Energy Storage, (2018). **20**: p. 30-40.

[7] González, A., et al., Review on supercapacitors: Technologies and materials. Renewable and Sustainable Energy Reviews, (2016). **58**: p. 1189-1206.

[8] Wang, F., et al., Latest advances in supercapacitors: from new electrode materials to novel device designs. Chemical Society Reviews, (2017). **46**(22): p. 6816-6854.

[9] Siniscalchi-Minna, S., et al., A non-centralized predictive control strategy for wind farm active power control: A wake-based partitioning approach. Renewable Energy, (2020). **150**: p. 656-669.

[10] Khan, M.I., et al., Improved photovoltaic performance of dye-sensitized solar cells by Au-ion implantation of titania film electrodes. Results in Physics, (2020). **17**: p. 103093.

[11] Bahadur, N.M., et al., Rapid synthesis, characterization and optical properties of TiO2 coated ZnO nanocomposite particles by a novel microwave irradiation method. Materials Research Bulletin, (2010). **45**(10): p. 1383-1388.

[12] Shanmugam, S.R., S. Adhikari, and R. Shakya, Nutrient removal and energy production from aqueous phase of bio-oil generated via hydrothermal liquefaction of algae. Bioresource technology, (2017). **230**: p. 43-48.

[13] Usman, M., et al., Facile synthesis of ironnickelcobalt ternary oxide (FNCO) mesoporous nanowires as electrode material for supercapacitor application. Journal of Materiomics, (2021).

[14] O'Neill, A., U. Khan, and J.N. Coleman, Preparation of High Concentration Dispersions of Exfoliated MoS2 with Increased Flake Size. Chemistry of Materials, (2012). **24**(12): p. 2414-2421.

[15] Li, X., et al., Orderly integration of porous TiO2(B) nanosheets into bunchy hierarchical structure for high-rate and ultralong-lifespan lithium-ion batteries. Nano Energy, (2017). **31**: p. 1-8.

[16] Aricò, A.S., et al., Nanostructured materials for advanced energy conversion and storage devices. Nature Materials, (2005). **4**(5): p. 366-377.

[17] Azman, N.H.N., et al., Graphene-based ternary composites for supercapacitors. International Journal of Energy Research, (2018). **42**(6): p. 2104-2116.

[18] Xie, S., et al., Nickel-cobalt selenide as high-performance and long-life electrode material for supercapacitor. Journal of Colloid and Interface Science, (2019). **540**: p. 306-314.

[19] Mahmood, N., et al., Graphene-based nanocomposites for energy storage and conversion in lithium batteries, supercapacitors and fuel cells. J. Mater. Chem. A, (2014). **2**(1): p. 15-32.

[20] Kim, B.K., et al., Electrochemical Supercapacitors for Energy Storage and Conversion, in Handbook of Clean Energy Systems. (2015). p. 1-25.

[21] Vangari, M., T. Pryor, and L. Jiang, Supercapacitors: Review of Materials and Fabrication Methods. Journal of Energy Engineering, (2013). **139**(2): p. 72-79.

[22] Li, Y., et al., Ni–Co sulfide nanowires on nickel foam with ultrahigh capacitance for asymmetric supercapacitors. J. Mater. Chem. A, (2014). **2**(18): p. 6540-6548.

[23] Sun, H.-Y., et al., Nickel precursor-free synthesis of nickel cobalt-based ternary metal oxides for asymmetric supercapacitors. Electrochimica Acta, (2018). **281**: p. 692-699.

[24] Palchoudhury, S., et al., Flexible Supercapacitors: A Materials Perspective. Frontiers in Materials, (2019). **5**(83).

[25] Cabeza, L.F., et al., 1 - Introduction to thermal energy storage systems, in Advances in Thermal Energy Storage Systems (Second Edition), L.F. Cabeza, Editor. (2021), Woodhead Publishing. p. 1-33.

[26] Kim, B., et al., Handbook of Clean Energy Systems. (2014). p. 1-25.

[27] May, G.J., A. Davidson, and B. Monahov, Lead batteries for utility energy storage: A review. Journal of Energy Storage, (2018). **15**: p. 145-157.

[28] Zhang, C., et al., Energy storage system: Current studies on batteries and power condition system. Renewable and Sustainable Energy Reviews, (2018). **82**: p. 3091-3106.

[29] Vangari, M., T. Pryor, and L. Jiang, Supercapacitors: Review of Materials and Fabrication Methods. Journal of Energy Engineering, (2013). **139**: p. 72-79.

[30] Sabzehmeidani, M.M., et al., Carbon based materials: a review of adsorbents for inorganic and organic compounds. Materials Advances, (2021). **2**(2): p. 598-627.

[31] Khan, I., K. Saeed, and I. Khan, Nanoparticles: Properties, applications and toxicities. Arabian Journal of Chemistry, (2019). **12**(7): p. 908-931.

[32] Syarif, N., T.A. Ivandini, and W. Wibowo, Direct synthesis carbon/Metal oxide composites for electrochemical capacitors electrode. Trans J Eng Manag Appl Sci Technol, (2012). **3**: p. 21-34.

[33] Cheng, Q., et al., Graphene and carbon nanotube composite electrodes for supercapacitors with ultra-high energy density. Physical Chemistry Chemical Physics, (2011). **13**(39): p. 17615-17624.

[34] Novoselov, K.S., et al., Electric field effect in atomically thin carbon films. Science, (2004) **306**(5696): p. 666-9.

[35] Zhu, Y., et al., Carbon-based supercapacitors produced by activation of graphene. Science, (2011). **332**(6037): p. 1537-41.

[36] Bhadra, S., et al., Progress in preparation, processing and applications of polyaniline. Progress in Polymer Science, (2009) **34**(8): p. 783-810.

[37] Rudge, A., et al., Conducting polymers as active materials in electrochemical capacitors. Journal of Power Sources, (1994). **47**(1): p. 89-107.

[38] Ren, L., et al., Three-Dimensional Tubular MoS2/PANI Hybrid Electrode for High Rate Performance Supercapacitor. ACS Applied Materials & Interfaces, (2015). **7**(51): p. 28294-28302.

[39] Chu, P. and L. Li, Characterization of amorphous and nanocrystalline carbon films. Materials Chemistry and Physics, (2006). **96**: p. 253-277.

[40] Karami, H., M. Mousavi, and M. Shamsipur, A New Design for Dry Polyaniline Rechargeable Batteries. Journal of Power Sources - J POWER SOURCES, (2003). **117**: p. 255-259.

[41] Eftekhari, A. and P. Jafarkhani, Polymerization of Aniline through Simultaneous Chemical and Electrochemical Routes. Polymer Journal, (2006). **38**(7): p. 651-658.

[42] Liu, X., et al., Design and fabrication of high performance flexible supercapacitor with polypyrrole@carbon fiber yarn electrode and redox active dopants. Synthetic Metals, (2021). **271**: p. 116654.

[43] Li, Y., et al., Facile preparation and enhanced capacitance of the polyaniline/sodium alginate nanofiber network for supercapacitors. Langmuir, (2011). **27**(10): p. 6458-63.

[44] Sawyer, D.T. and J.S. Valentine, How super is superoxide? Accounts of Chemical Research, (1981). **14**(12): p. 393-400.

[45] Liu, R., et al., Fundamentals, Advances and Challenges of Transition Metal Compounds-based Supercapacitors. Chemical Engineering Journal, (2021). **412**: p. 128611.

[46] Sun, H., et al., Nanostructure Nickel-Based Selenides as Cathode Materials for Hybrid Battery-Supercapacitors. Frontiers in Chemistry,(2021). **8**.

47] Sun, H., et al., Nanostructure Nickel-Based Selenides as Cathode Materials for Hybrid Battery-Supercapacitors. Frontiers in chemistry, (2021). **8**: p. 611032-611032.

[48] Chebrolu, V., et al., Selective Growth of Zn–Co–Se Nanostructures on Various Conductive Substrates for Asymmetric Flexible Hybrid Supercapacitor with Enhanced Performance. Advanced Materials Technologies, (2019). **5**.

[49] Lu, T., et al., Fabrication of transition metal selenides and their applications in energy storage. Coordination Chemistry Reviews, (2016). **332**.

[50] Mohamed, A.M. and N.K. Allam, Transition Metal Selenide (TMSe) electrodes for electrochemical capacitor devices: A critical review. Journal of Energy Storage, (2021): p. 103565.

[51] Miao, C., et al., Facile Synthesis of Metal–Organic Framework-Derived CoSe2 Nanoparticles Embedded in the N-Doped Carbon Nanosheet Array and Application for Supercapacitors. ACS Applied Materials & Interfaces, (2020). **12**(8): p. 9365-9375.

[52] Ye, B., et al., Coelectrodeposition of NiSe/ZnSe Hybrid Nanostructures as a Battery-Type Electrode for an Asymmetric Supercapacitor. The Journal of Physical Chemistry C, (2020). **124**(39): p. 21242-21249.

[53] Peng, H., et al., A novel aqueous asymmetric supercapacitor based on petal-like cobalt selenide nanosheets and nitrogen-doped porous carbon networks electrodes. Journal of Power Sources, (2015). **297**: p. 351-358.

[54] Wu, S., et al., One-step solvothermal synthesis of nickel selenide nanoparticles as the electrode for high-performance supercapacitors. Journal of Alloys and Compounds, (2019). **784**: p. 347-353.

[55] Zhang, X., et al., All-solid-state asymmetric supercapacitor based on porous cobalt selenide thin films. Journal of Alloys and Compounds, (2019). **772**: p. 25-32.

[56] Xia, C., et al., Asymmetric supercapacitors with metal-like ternary selenides and porous graphene electrodes. Nano Energy, (2016). **24**: p. 78-86.

[57] Zhang, Y., et al., Self-templated synthesis of N-doped CoSe2/C double-shelled dodecahedra for high-performance supercapacitors. Energy Storage Materials, (2017). **8**: p. 28-34.

[58] Du, L., et al., Ternary nickel-cobalt selenide nanosheet arrays with enhanced electrochemical performance for hybrid supercapacitors. Journal of Alloys and Compounds, (2019). **778**: p. 848-857.

[59] Willard, H.H., et al., Instrumental methods of analysis, 7th edition. (1988), United States: Wadsworth Publishing Company.

[60] Goldstein, J.N.D.E.M.J.R.R.N.W.M.S.J.H.J.J.D.C., Scanning electron microscopy and x-ray microanalysis. (2018), New York, NY: Springer.

[61] Condon, J.B., Chapter 3 - Interpreting the Physisorption Isotherm, in Surface Area and Porosity Determinations by Physisorption, J.B. Condon, Editor. (2006), Elsevier Science: Amsterdam. p. 55-90.

[62] Condon, J.B., Chapter 2 - Measuring the Physisorption Isotherm, in Surface Area and Porosity Determinations by Physisorption, J.B. Condon, Editor. (2006), Elsevier Science: Amsterdam. p. 29-53.

[63] Rootare, H.M. and C.F. Prenzlow, Surface areas from mercury porosimeter measurements. The Journal of Physical Chemistry, (1967). **71**: p. 2733-2736.

[64] Zamora-Sequeira, R., et al., What are the Main Sensor Methods for Quantifying Pesticides in Agricultural Activities? A Review. Molecules (Basel, Switzerland), (2019). **24**(14): p. 2659.

[65] Rohrbach, F., et al., Label-free impedimetric aptasensor for lysozyme detection based on carbon nanotube-modified screen-printed electrodes. Anal Biochem, (2012). **421**(2): p. 454-9.

[66] Beitollahi, H., F.G. Nejad, and S. Tajik, 12 - Application of magnetic nanomaterials as electrochemical sensors, in Magnetic Nanomaterials in Analytical Chemistry, M. Ahmadi, A. Afkhami, and T. Madrakian, Editors. (2021), Elsevier. p. 269-301.

[67] Solhi, E. and M. Hasanzadeh, Critical role of biosensing on the efficient monitoring of cancer proteins/biomarkers using label-free aptamer based bioassay. Biomedicine & Pharmacotherapy, (2020). **132**: p. 110849.

[68] de-los-Santos-Álvarez, N., et al., Modified-RNA Aptamer-Based Sensor for Competitive Impedimetric Assay of Neomycin B. Journal of the American Chemical Society, (2007). **129**(13): p. 3808-3809.

[69] Bogomolova, A., et al., Challenges of electrochemical impedance spectroscopy in protein biosensing. Anal Chem, (2009). **81**(10): p. 3944-9.